



A simultaneous planar laser-induced fluorescence, particle image velocimetry and particle tracking velocimetry technique for the investigation of thin liquid-film flows



Alexandros Charogiannis, Jae Sik An, Christos N. Markides*

Clean Energy Processes (CEP) Laboratory, Department of Chemical Engineering, Imperial College London, London SW7 2AZ, United Kingdom

ARTICLE INFO

Article history:

Received 26 March 2015

Received in revised form 22 May 2015

Accepted 8 June 2015

Available online 14 June 2015

Keywords:

Planar laser-induced fluorescence

Particle image velocimetry

Particle tracking velocimetry

Harmonically excited films

Film thickness

Velocity profile

ABSTRACT

A simultaneous measurement technique based on planar laser-induced fluorescence imaging (PLIF) and particle image/tracking velocimetry (PIV/PTV) is described for the investigation of the hydrodynamic characteristics of harmonically excited liquid thin-film flows. The technique is applied as part of an extensive experimental campaign that covers four different Kapitza (Ka) number liquids, Reynolds (Re) numbers spanning the range 2.3–320, and inlet-forced/wave frequencies in the range 1–10 Hz. Film thicknesses (from PLIF) for flat (viscous and unforced) films are compared to micrometer stage measurements and analytical predictions (Nusselt solution), with a resulting mean deviation being lower than the nominal resolution of the imaging setup (around 20 μm). Relative deviations are calculated between PTV-derived interfacial and bulk velocities and analytical results, with mean values amounting to no more than 3.2% for both test cases. In addition, flow rates recovered using LIF/PTV (film thickness and velocity profile) data are compared to direct flowmeter readings. The mean relative deviation is found to be 1.6% for a total of six flat and nine wavy flows. The practice of wave/phase-locked flow-field averaging is also implemented, allowing the generation of highly localized velocity profile, bulk velocity and flow rate data along the wave topology. Based on this data, velocity profiles are extracted from 20 locations along the wave topology and compared to analytically derived ones based on local film thickness measurements and the Nusselt solution. Increasing the waviness by modulating the forcing frequency is found to result in lower absolute deviations between experiments and theoretical predictions ahead of the wave crests, and higher deviations behind the wave crests. At the wave crests, experimentally derived interfacial velocities are overestimated by nearly 100%. Finally, locally non-parabolic velocity profiles are identified ahead of the wave crests; a phenomenon potentially linked to the cross-stream velocity field.

© 2015 The Authors. Published by Elsevier Inc. This is an open access article under the CC BY license (<http://creativecommons.org/licenses/by/4.0/>).

1. Introduction

1.1. Problem definition and motivation

Falling film flows, defined as liquid films falling freely under the action of gravity alone, are important canonical free-surface flows that are encountered in a wide range of industrial applications, such as wetted-wall absorbers, heat exchangers, condensers, evaporators and reactors, predominantly owing to their high surface-to-volume ratios and associated high heat and mass transfer capabilities even at modest flow-rates. Commonly employed geometries involve liquid films flowing down vertical or inclined

flat plates and annular or square cross-section tubes. They also appear in oil and gas applications in the limit of low (or, zero) gas flow-rates in vertical or inclined pipelines.

Extensive theoretical and experimental investigations have suggested that the rates of heat and mass transfer in these flows are strongly linked to the spatiotemporal variations of the hydrodynamic characteristics of the films, and in particular the waviness of the gas–liquid interface (Brauner and Maron [1], Mudawar and Houpt [2], Alekseenko et al. [3]). Yet, despite the numerous and well-performed experimental studies encountered in literature, only a limited number of publications relating to the simultaneous and spatiotemporally resolved variations of film thickness and velocity are currently available; a limitation linked inherently to the many challenges that arise when performing these measurements. The restricted fluid domains under observation (often

* Corresponding author.

E-mail address: c.markides@imperial.ac.uk (C.N. Markides).

sub-mm) and the intermittent nature of the moving and complex waves on the interface render the extraction of reliable information particularly challenging. The present study is therefore motivated by the strong desire for simultaneous, detailed space- and time-resolved film thickness and velocity field data underneath the interfacial wave structures in falling film flows. Such measurement data can constitute an important springboard towards unlocking the mechanisms behind the development and interaction of interfacial instabilities that can be harnessed to enhance further heat and mass transfer rates in related flows and practical processes, while facilitating the development and validation of advanced and accurate analytical and numerical modelling efforts.

1.2. Review of experimental methods

Before proceeding to a statement of the specific aims and objectives of the present effort, this section reviews suitable measurement techniques, with particular emphasis on the application of optical methods. The latter have gradually penetrated a wide and diverse range of scientific research fields, including fluid mechanics, aerodynamics, heat and mass transfer, as well as reacting flows and combustion, while advancing considerably our understanding of flows in these areas with progressively more detailed information over the past few decades.

Experimental investigations of films flows can broadly be classified as being intrusive or non-intrusive according to the practice adopted in obtaining the desired data. In reference to the first category, conductivity probes and hot wire anemometry (HWA) were employed by Ishigai and Nakanisi [4] in classifying the flow regimes observed in vertically falling films, based on film thickness measurements. HWA was also employed by Ueda and Tanaka [5] in their study of spindle oil films flowing down an inclined plate over the 3000–6000 Reynolds (Re) number range, and by Lyu and Mudawar [6] in their statistical investigation of the interaction between film waviness and heat transfer ($Re = 2700$ – 11700). Conductivity probes were utilized in wave height measurements by Nosoko et al. [7] and the generation of film thickness statistics by Karapatsios et al. [8] and Belt et al. [9]. The limited spatial resolution and intermittent exposure of these probes to the films (and consequent disturbance thereof) can introduce measurement uncertainties, which can be avoided by employment of alternative, non-intrusive practices such as optical methods. Another non-intrusive but non-optical instrument class that has frequently been favoured are capacitance probes (see for example Yu et al. [10], Brauner and Maron [1], Ambrosini et al. [11] and Zhao et al. [12]). In this case, complicated calibration procedures along with a limited spatial resolution can limit their use, depending on what is required.

Optical diagnostics have been applied extensively to the study of liquid and gaseous flows, as they allow for non-invasive real-time imaging and interpretation of one, two or three-dimensional spatial distributions of seeded or naturally occurring tracers or particles. Investigations of unsteady interfacial flows, and in particular liquid films, have also been attempted with a broad range of optical methods. In one such method, a molecular-tagging approach is employed whereby a small quantity of a fluorescing dye is dissolved in an optically transparent liquid. Following irradiation by a laser source or high intensity lamp, a red-shifted emission (fluorescence) is observed; the collection of the fluorescence signal by a detector such as a camera allows for the visualization of the illuminated region of the flow. The fluorescence and phosphorescence (molecular de-excitation from a triplet to a singlet state) emission of biacetyl were, for example, used by Schagen and Modigell [13] to investigate oxygen diffusion in films falling down a 4° (to the horizontal) incline at $Re = 177$. Later, the sensitivity of the time-integrated phosphorescence signal to

temperature variations was exploited in heat transfer studies (Schagen et al. [14], Schagen and Modigell [15]). Liu et al. [16] investigated the evolution of primary instabilities of aqueous glycerol solutions, also at shallow angles, by illuminating the flow field from above and observing the laser-induced fluorescence (LIF) emission with a CCD camera from below a transparent substrate. The fluorescence intensity was calibrated for film height, allowing the authors to quantify film thickness over an extended two-dimensional (2-D) domain, and establish a phase boundary between flow regimes characterized by saturated finite amplitude waves and multi-peaked solitary waves. Using the same technique, Liu and Gollub [17] investigated inelastic interactions between solitary wave pulses over a range of excitation frequencies and conditions (i.e., Re). The breakdown of periodic 2-D waves and interactions thereof with both sideband and sub-harmonic secondary 2-D instabilities (Liu and Gollub [18]), as well as the nature of three-dimensional (3-D) instabilities (Liu et al. [19]) formed the central thesis of two more contributions, highlighting the wealth of information made available by the employment of LIF imaging. Other groups have also employed the same measurement technique, for example Vlachogiannis and Bontozoglou [20] and Alekseenko et al. [21]. Using Rhodamine 6G as the fluorescent marker, high-speed imaging and continuous-wave lasers, Alekseenko and co-workers have carried out extensive fluorescence-based investigations over a wide range of downwards annular flows (Alekseenko et al. [22–24]). For the upper range of the liquid Re range examined ($Re = 18$ – 350), the authors captured the formation of disturbance waves (primary waves) with non-uniform height along the circumference of a pipe, and deduced that this non-uniformity affects the generation of ripples (secondary waves). The same technique was later applied to the study of gas (shear)-driven liquid flows in a horizontal rectangular duct, providing additional qualitative evidence for the proposed mechanism for ripple generation observed in their earlier downwards annular flow experiments (Cherdantsev et al. [25]).

As an alternative to fluorescence intensity (LIF) based measurements, planar illumination across a flow field can be used to resolve spatiotemporal film thickness variations over a 2-D domain by the deployment of planar laser-induced fluorescence (PLIF) imaging. The primary difference between this and the former approach is that one or both liquid film boundaries need to be identified in the fluorescence images in order to produce a measurement of the spatial extent of the film. Clearly, the advantage in this case is that the flow within the film can be visualized, allowing for spatiotemporally resolved velocity (in conjunction with the utilization of velocity tracers) or temperature data to be obtained, and liquid–liquid interfaces to be identified. PLIF, for example, has been employed to provide film thickness information in downwards annular flows (Zadrazil et al. [26]) and phase information in horizontal liquid–liquid flows (Morgan et al. [27]). Furthermore, Mathie et al. [28,29] employed Rhodamine B PLIF alongside infrared (IR) imaging to study the spatiotemporal film thickness and heat transfer coefficient (HTC) variations over an inclined heated plate over a range of flow conditions (Re , forcing frequencies and heat fluxes). They showed that despite the fact that the steady flow analysis describes the correlation between film thickness and HTC reasonably well, significantly higher (by up to a factor of two) HTC enhancements ensue at low mean film thickness. It should be noted that this is not the only study where the employment of Rhodamine B for thermographic purposes has been favoured (see for example Chamrathy et al. [30]), as the particular tracer offers excellent temperature sensitivity even at near-room temperatures, a high fluorescence quantum yield, and is relatively non-toxic.

Another popular optical method relevant to the retrieval of film thickness data is chromatic confocal imaging (CCI). Originally used

for the surface structure characterization of solids, this method exploits the operating principles of confocal imaging in combination with the chromatic aberration of lens optics in order to generate a continuous spectrum of monochromatic light from a polychromatic source. A spectrometer measures the intensity distribution of the reflected signal off the gas–liquid interface, and the dominant frequency provides a measurement of the position of the interface within the field of view of the detector. Amongst the advantages of CCI, the high sampling rates, spatial resolution and accuracy on offer clearly stand out, with reduced sensitivity in the presence of gradients constituting the main drawback. Lel et al. [31] conducted a comparative assessment between CCI and LIF imaging based on signal intensity for a wide range of film flow conditions and observed good agreement amongst the two techniques, as well as other data available in literature. CCI was later applied alongside laser Doppler velocimetry (LDV) and micro-PIV (particle image velocimetry) in a pair of outstanding, combined experimental–numerical investigations dedicated to the identification of backflow (Dietze et al. [32]) and flow separation (Dietze et al. [33]) in laminar falling films. A more detailed account of the findings of both contributions will be provided later on, as the fundamental novelty of their work lies with the application of optical velocimetry techniques, a brief review of which will be presented in the following paragraphs.

A distinction between particle-seeded and molecular-tagging optical velocimetry techniques is hereby made in order to better structure the material provided in this part of the introductory section. The photochromic dye activation (PDA) technique, which has been extensively used to investigate the hydrodynamics of liquid films, stands for a prime example of the former. Introduced by Popovich and Hummel [34] as a novel non-intrusive tool for recovering velocity distributions within liquid flows, and later adapted by Ho and Hummel [35] for the study of laminar and turbulent films, PDA has proven to be relatively simple to implement, in light of the aforementioned challenges inherent to experiments in thin liquid-film flows. Upon illumination by a light source, for example an ultraviolet (UV) laser, thin fluorescing traces arranged perpendicular to the direction of the flow are generated, serving as local markers of the fluid motion and allowing for direct velocity profile measurements. Typically applied alongside back-illuminated high-speed photography, PDA-based turbulent flow visualization experiments have been carried out by Karimi and Kawaji with the ultimate goal of characterizing a wide range of two-phase flows, including counter-current annular flows (Karimi and Kawaji [36]), slug and stratified flows (Kawaji et al. [37]), freely falling films down a vertical tube (Karimi and Kawaji [38]) and falling films with counter-current shear gas flow (Karimi and Kawaji [39]). More recently, Moran et al. [40] investigated the flow dynamics of laminar films flowing down a 45° incline ($Re = 11$ – 220), and noted significant over-predictions of the time-averaged mean and maximum velocities by the Nusselt theory (gravity–viscosity equilibrium).

Aside from molecular tagging, time-resolved velocity measurements at a single point in the flow can be obtained by laser Doppler velocimetry (LDV); essentially a local measurement of the Doppler shift between the light (typically from a continuous-wave laser source) incident and scattered from seeded or naturally occurring particles within an interrogated volume. Mudawar and Houpt [2] conducted LDV measurements in their study of mass and momentum transport in thick aqueous propylene glycol films ($Re = 209$ – 414), and demonstrated a reduced velocity field sensitivity to the presence of large amplitude waves with increasing substrate thickness. Dietze and co-workers (Dietze et al. [32,33]) employed LDV alongside CCI and subsequently micro-PIV in their studies of backflow and flow separation in inclined and vertically falling films. In the first case, LDV produced near-zero axial velocity data close to

the wall, while in the second, negative velocities ensued in the capillary wave region confirming the presence of local backflow.

In contrast to LDV, particle image velocimetry (PIV) and particle tracking velocimetry (PTV) allow for 2-D velocity vector maps to be generated (tomographic extensions are capable of full 3-D volumetric measurements, although here we focus on planar measurements). These techniques are based on tracking the motion of seeded particle groups (PIV) or individual particles (PTV), by sequential illumination and imaging of scattering or fluorescence signals within a small time-interval. The obtained image-pairs are subsequently processed, typically by using multi-pass cross-correlation approaches. Choosing amongst the two techniques is typically based on resolution requirements (with PTV offering superior resolution, albeit at the cost of increased processing time), as well as accuracy and statistical conversion, depending also on the presence or lack of strong gradients within the probed region of the flow. In the case of PIV, the presence of gradients can introduce severe bias errors; for film flow investigations, this applies especially to the near-wall regions, with PTV or micro-PIV rendered as superior options. A comprehensive review of modern particle-based velocimetry practices can be found in the book by Raffel et al. [41]. Finally, prior to commencing with a brief review of contemporary investigations employing PIV and PTV, it is essential to note a study by Alekseenko et al. [42], whereby the formation and evolution of waves on a vertically falling liquid film was studied by simultaneous application of the shadow method (for film thickness determination) and stroboscopic particle visualization (for velocity measurements). The combined optical technique allowed, for the first time, the retrieval of instantaneous velocity profiles along the wave topology, a practice that constitutes one of the main objectives of the current study as well.

Schubring et al. [43] employed fluorescing particles (mean particle diameter of 3 μm) in their effort to address the validity of the universal velocity profile (UVP) in horizontal gas–liquid flows by conducting micro-PIV measurements. Their results show that the base-film-zone velocity profile is linear and extends farther from the wall than the single-phase turbulent flow case suggests, while significantly higher axial velocities and fluctuation intensities are observed in the wave zone. Similarly, in the case of co-current horizontal flows between two immiscible liquids in a circular pipe, the application of PTV enabled Morgan et al. [44] to quantitatively assess the velocity profiles in the lower heavier liquid-layer (aqueous glycerol solution), the mixing layer, and the upper lighter liquid-layer (aliphatic hydrocarbon oil). For the range of examined superficial velocities, the axial velocity profiles in the zone occupied by the aqueous glycerol solution were characteristic of laminar flows whereas in the region occupied by oil assumed a shape typical of turbulent flows. An interesting study by Alekseenko et al. [45] presented results from PIV-based flow field investigations inside wavy rivulets flowing down the underside of a slightly inclined circular pipe ($Re = 7.9$ – 20.3). Vortex flows were consistently observed within the wave humps, with pronounced deviations from the self-similar profile. The hydrodynamics of waves in laminar, unforced (unpulsed) vertically falling films and downwards co-current gas–liquid annular flows have also recently been studied by the employment of fluorescence imaging simultaneously with micro-PIV and PIV/PTV respectively. In the first case, and despite the observation of parabolic profiles throughout the investigated Re range (27–200), strong deviations from the Nusselt velocity profile predictions were noted depending on film topology, while wave interactions at the higher end of the investigated Re range lead to the formation of turbulent spots (Adomeit and Renz [46]). With regards to downwards co-current gas–liquid annular flows, the PTV-derived velocity data by Zadrzil et al. [47] revealed the presence of multiple recirculation zones within disturbance waves that may be linked to liquid entrainment, and

mass and momentum transfer from the near-wall zone towards the gas–liquid interface.

An attempt to address the deficits of standard PIV in thin-film flow investigations was recently made by Ashwood et al. [48]. By borrowing strategies from micro-PIV (mainly with regards to seeding and imaging), the authors provided mean velocity profile data in a co-current upward flow, although in a rectangular duct, suggesting that certain modifications to the UVP must be implemented before a meaningful approximation of the profiles can be made. In a separate effort, Dietze et al. [33] also applied micro-PIV in the capillary wave region of falling annular-film flows, and linked changes in the film surface curvature and ensuing adverse pressure-gradients to an observed backflow in the first capillary minimum and flow deceleration in the second capillary minimum. This experimental evidence was complemented by numerical simulations.

1.3. Aims and objectives

The above presentation of modern experimental practices is not intended as an exhaustive summary thereof, but only to serve as an indication of selected publications of relevant practices that are being applied to the fundamental, detailed understanding of thin film-flows stems. From this background, we proceed towards the primary aim of this contribution, which is to establish a suitable experimental methodology for characterizing simultaneously the interfacial dynamics and the velocity fields within wavy thin films over a wide range of flows conditions in a spatially and temporally resolved manner. In more detail, the present experimental campaign aims to provide a characterization of the spatiotemporal variation of the film thickness, wave velocity, interfacial velocity and two-dimensional velocity distribution within isothermal liquid films developing over the surface of an inclined flat glass plate. As was noted earlier, the primary objective of this contribution is to establish the methodology behind the combined optical technique, conduct an uncertainty analysis and present validation results and sample study cases illustrative of the wealth of information that becomes available. Overall, the experimental campaign comprises four different Kapitza (Ka) number liquids, Re spanning the range 2.3–320, and forcing frequencies in the range 1–10 Hz.

Following a description of the arrangement employed in these experiments in Section 2, a detailed account of the experimental methodology developed for the simultaneous application of PLIF and PIV/PTV measurements is provided in Section 3. Following this, in Section 4, the effectiveness of this methodology is demonstrated by presenting comparative measurements of both film thickness and velocity data to independent, experimentally derived data and steady flow analytical results for flat-film flows. Select film topology, statistical results and time-averaged axial velocity profiles are presented in tandem to highlight the benefits of simultaneously employing thickness and velocimetry techniques, while a methodology and sample results for generating moving frame-of-reference wave/phase-locked average two-dimensional velocity maps within a wave are outlined. The results are also compared with the steady Nusselt-flow theory and literature data. Prior to commencing with a description of the experimental setup, it is essential to define the two primary dimensionless numbers of the flows considered in this study. The Reynolds number, Re , provides a quantitative expression for the relative significance between inertial and viscous forces, and is defined in terms of a characteristic flow velocity U , dimension D and the kinematic viscosity of the fluid ν_f :

$$Re = \frac{UD}{\nu_f}. \quad (1)$$

The Kapitza number expresses the dimensionless ratio between surface tension and inertial forces, and acts as an indicator of the hydrodynamic wave regime:

$$Ka = \frac{\sigma_f}{\rho_f \nu_f^{4/3} (\sin(\theta)g)^{1/3}}, \quad (2)$$

where σ_f stands for the liquid surface tension, ρ_f is the liquid density, θ is the inclination angle of the substrate to the horizontal, and g is the gravitational acceleration.

2. Experimental setup

2.1. Flow loop

A schematic representation of the experimental configuration, which is an evolution of a previously employed setup (Mathie

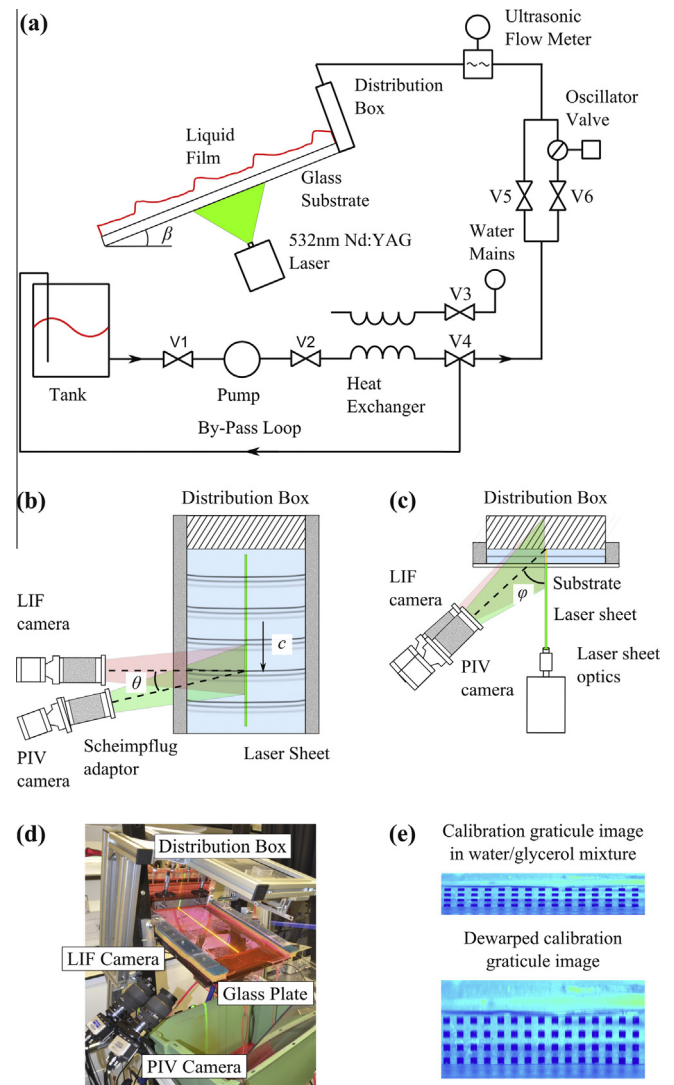


Fig. 1. (a) Schematic of the liquid flow-loop comprised of the test section, pump, heat exchanger, oscillator valve and bypass loop. (b) Schematic of the test section showing the orientation of the laser sheet and collection optics from top. The angle θ was varied in the 13–17° range throughout the experimental campaign. (c) Schematic of the test section showing the orientation of the laser sheet and collection optics from the front. The angle ϕ was varied in the 34–38° range throughout the experimental campaign. (d) Photograph of the test section. (e) Section of the calibration graticule image in aqueous glycerol solution (top) and in aqueous glycerol solution following refractive and perspective distortion corrections (bottom).

et al. [28,29]), is given in Fig. 1(a). The setup consists of a planar test section over which liquid-film flows develop, and a closed-loop circuit via which the liquid circulates. A closed as opposed to an open-loop circuit is selected so that the fluorescent dye and PIV particle concentrations remain constant throughout the duration of the experiments.

The tank located underneath the test section acts as a temporary reservoir for the liquid flowing around the loop. When not in operation, this assumes the role of a storage reservoir. When in operation, the flow passes through a counter-flow heat-exchanger supplied by Alfa Laval to extract the heat imparted to the fluid due to pumping and keep the liquid at a constant temperature; despite the fact that no heating is imposed onto the liquid films, the temperature of the fluid rises from room (around 25 °C) to 30 °C within a few minutes of operation even at intermediate flow-rates for high viscosity aqueous solutions. Therefore, the employment of a cooling system is rendered necessary. The heat exchanger cooling line is fed by mains water and the heat extraction rate is modulated by adjusting the water flow-rate (Valve V3). It was found, by monitoring the temperature inside the distribution box in this way, that the liquid temperature can be maintained to within 0.5 °C in the apparatus over the course of an experimental run.

Valves V1 and V2 are used to isolate the pump (Grundfos CHI 4-30) from the rest of the loop when, for example, replacing the liquid mixture, while Valve V4 is employed for bypassing part of the flow back to the tank. This allows a higher flow-rate to be maintained through the pump, reducing the likelihood of stalling and cavitation, thus allowing for more efficient operation of the heat exchanger, and therefore more accurate temperature control. The rotational speed of the pump is controlled by a 1200 VA variable autotransformer (Carroll & Meynell).

After the bypass valve, the flow is split into two separate, parallel lines; a steady and a pulsating supply component. The pulsating supply is generated by diverting a portion of the total flow through a mechanically oscillating valve. The oscillating valve comprises a metallic spindle with a hole drilled transversely through it (throttle), rotating within the valve body. Torque is provided to the throttle valve by a 5 V, 1 A, 1.8° step-angle stepper motor controlled by an in-house developed controller. The TTL pulse output of a TTI TG315 function generator was used to regulate the rotational speed of this valve, achieving a maximum speed of approximately 370 rpm (corresponding to a wave frequency of slightly above 11 Hz). Following the oscillating valve, the two supplies recombine prior to entering the distribution box. The reason for employing this setup is to achieve better control over the wave frequency and amplitude, selectively triggering the rapid growth of regular waves and fully developed wave regimes within the confines of a short test section.

Finally, an ultrasonic flow meter (UF25B by Cynergy3 Components) is installed after the throttle valve but prior to the distribution box. This particular component operates by measuring the transit time between ultrasonic pulses propagating along and against the direction of the flow, and generates an electronic pulse for every mL passing through it. The flowmeter output is recorded by a National Instruments data acquisition system (NI USB-6211) operated using MATLAB and triggered by output TTL pulses generated by the laser. The recorded pulse sequences are then used to reconstruct the instantaneous flow-rate and cumulative volumetric flow time-traces, from which the mean flow-rate and intensity of pulsation can be determined. The average flow-rate is calculated by either dividing the total liquid volume by the sampling time, or by averaging the instantaneous flow-rate time trace; both approaches return the same result. The peak amplitude of pulsation is estimated as one half of the average disparity between local flow-rate maxima and minima, while the intensity of pulsation is

obtained by dividing the peak amplitude by the mean flow-rate. Using Valve V6 which allowed control of the intensity of pulsation to within a few percentage points, the latter is varied between 5% and 10% depending on the forcing frequency. It should also be noted that preliminary experimental runs have shown neither the wave characteristics, nor the wave crest height, trough height or mean film height are affected when varying the intensity of pulsation in the 5–20% range.

2.2. Test section

The test section comprises a 400 × 285 mm soda-lime glass plate of 0.7-mm thickness (Instrument Glasses) and is mounted on an aluminium support frame. Support to the glass is provided along its periphery in order to maximize the optically accessible area. Hinges installed on either side of the frame allow for adjustment of the test section inclination angle (β), presently set to 20°. This particular experimental parameter is of outmost importance when investigating the dynamics of film flows; however, since the objective of the present experimental effort is to establish a combined PLIF and PIV/PTV optical imaging methodology, and examine the effects of Re and Ka , as well as that of forcing frequency on isothermal film-flow dynamics, the inclination angle was not varied.

A flow distribution box acting as a settling chamber and comprised of meshes and a honeycomb is installed at the top of the test section in order to uniformly dispense the flow across the span of the plate, as well as to break down and dissipate large-scale eddies. The exit of the box/chamber is equipped with a knife-edge, the height of which (D) can be adjusted by a pair of micrometer stages. This regulates the flow contraction and prevents the generation of a hydraulic jump or air flowing back into the box.

Prior to each measurement run, the distribution box is manually primed using a syringe, while a type-K thermocouple is installed allowing for the liquid temperature to be monitored. A calibrated Omega microprocessor thermometer is employed in measuring the liquid temperature. The Reynolds number mentioned earlier is evaluated here at the flow inlet, by using the mean volumetric flow-rate (measured by the ultrasonic flowmeter) per unit width of the channel (285 mm), Γ , (Eq. (3)):

$$Re = \frac{DU}{\nu_f} = \frac{\Gamma}{\nu_f}. \quad (3)$$

In the above definition, which is throughout this paper, U stands for the liquid bulk velocity at the film-flow inlet (i.e., the location at the exit of the distribution box where the film flow is introduced over the plate/substrate) and D is the channel depth at the same location as set by the knife-end and micrometer stages.

As can be observed by inspecting Fig. 1(a), the dye-doped liquid flowing down the inclined glass plate is excited from the wall-side (underneath) rather than the free film surface. The benefits of adopting this particular arrangement are instrumental with regards to the successful realization of the proposed combined PLIF and PIV/PTV diagnostic strategy; if the moving wavy free surface had been illuminated instead, the incident laser-sheet light would have been subjected to strong, spatially and temporally non-uniform beam stirring and lensing. In addition to the illumination of the film flows, the imaging is also carried out from underneath the test section, as shown in Fig. 1(c) and (d). Again, this arrangement is preferred in order to limit the presence of out-of-plane reflections within the field of view of the collection optics, and optical distortions experienced by the reflected and fluorescing light along the line-of-sight of the cameras, therefore not necessitating any further image corrections.

2.3. Laser and imaging setup

A double-cavity frequency-doubled Nd:YAG laser (Nano-L-50-100PV by Litron Lasers) is used to excite the Rhodamine-B-seeded liquid at a rate of 100 Hz. The maximum available laser energy at the second harmonic of the laser, i.e., 532 nm, is approximately 50 mJ/pulse. Sheet optics with a 10° -divergence are employed in forming a thin (approximately 200 μm) sheet extending along the length of the glass plate. The collection optics comprise two LaVision VC-Imager Pro HS 500 CMOS cameras, one used for the PLIF measurement and one for the PIV measurements. The camera pixel size corresponds to $12 \times 12 \mu\text{m}$, the sensor size to $15.4 \times 12.3 \text{ mm}$ (1280×1024 pixels), the bit depth to 10 bit, the maximum frame rate to 500 Hz, and the quantum efficiency to 40%. Both cameras are equipped with Sigma 105 mm f/2.8 Macro lenses, and 32-mm extension rings in order to achieve the desired magnification (imaging region along the film corresponds to approximately 33 mm). In addition, a Scheimpflug adaptor is installed on the PIV camera which is positioned at a slight angle relative to the imaging plane. The latter, and consequently, part of the imaging region along the direction of the flow is out of focus. Both cameras and lasers are synchronized by a LaVision High-Speed Controller (HSC), operated using the LaVision DaVis 8.2.1 software.

A particularly challenging aspect of optical diagnostics in this type of configuration for the measurement of film flows is that of correcting for optical distortions stemming from the refractive index mismatch between the liquid and the transparent solid substrate responsible for supporting the flow and allowing for optical access (see, for example Budwig [49]). In addition, optical distortions often arise on account of geometrical features or restrictions associated with the solid domain; for example, in the case of annular flows, no solid surface parallel to the imaging plane is available (Zadrazil et al. [26]). It has, therefore, become common practice to employ a “correction box”, which is a transparent component either solid or hollow and filled with a transparent liquid, in order to alleviate the aforementioned distortion sources. The advantage of the particular approach is that despite the correction performed, the imaging system resolution is preserved, although this comes at the cost of refractive index restrictions imposed on the fluid selection. In other words, the liquid is largely selected on the basis of matching the refractive index of the correction box material as well, rather than based on its properties (such as the viscosity and surface tension) alone. For the purposes of the present experiments for which the variation of Ka by tailoring the viscosity, surface tension and density of the liquid is a primary objective, the implementation of an alternative approach is necessary. Prior to the undertaking of the final simultaneous PLIF–PIV/PTV measurements, the imaging planes of both cameras are mapped and corrected for perspective distortions using a calibration graticule immersed inside the employed liquid mixture. For this purpose, a Perspex box with its bottom surface removed (the surface that would otherwise adhere to the glass plate) is carefully positioned at the imaging plane using a micrometer stage, and subsequently filled with the liquid mixture through a hole at its top surface using a syringe. In this way, an accurate scaling of the PLIF–PIV imaging domain can be performed for a wider selection of liquids. Calibration graticule images obtained by implementing the above-described procedure are shown in Fig. 1(e). Mapping and optical distortion corrections for the two-camera setup are performed using a pinhole model available in DaVis. The camera pinhole model constitutes a simplified description of the mathematical relationship between the coordinates of a point on the object plane, in this case the illuminated film region, and its projection onto the image plane, in this case the CMOS sensor. The camera aperture is modelled as a pinhole, while it is further

assumed that no lenses are employed in order to focus the image of the real object. The resulting apparent resolution was between 28.0 $\mu\text{m}/\text{pixel}$ and 29.7 $\mu\text{m}/\text{pixel}$ for the four experimental runs (i.e., four different fluids and Ka), with a root mean square (RMS) error of 0.5–0.9 pixels.

Another key aspect of the simultaneous implementation of PLIF and PIV/PTV imaging concerns the appropriate camera filter selection. A short-pass filter (Edmund Optics, part number 84-721) with a cut-off frequency at 550 nm is installed on the PIV, making the entire visible spectrum below 550 nm accessible for camera calibration purposes. For the purposes of PLIF imaging, a long-pass optical filter purchased from LaVision (cut-off frequency at 540 nm) is utilized instead. The dye (Rhodamine B purchased from Sigma–Aldrich) at a concentration of approximately 0.5 g/L is used, while glass hollow spheres (LaVision, 11.7 μm mean diameter, 1.1 g/cm³ density) are seeded at a concentration of approximately 0.18 g/L (approximately 2×10^8 particles/L) for tracking the fluid motion. The Stokes number St , defined as the ratio of the particle motion characteristic time scale to the flow characteristic time scale was estimated for a range of flow conditions on the following basis: Flow characteristic time scales were calculated using the smallest length scales (capillary wave lengths) and the highest interfacial velocities (wave crest interfacial velocities) encountered in the examined flows, thus adopting a most conservative approach. These were of the order of 10^{-2} – 10^{-3} s, corresponding to St numbers also of the order of 10^{-3} ($\ll 1$) in the worst case. Hence, it can be assumed that the particles follow the flows faithfully.

3. Experimental methodology

3.1. PLIF data acquisition and processing

The PLIF camera is operated in dual-frame mode (like the PIV camera), so that for every PIV frame, a corresponding PLIF frame is acquired. The interframe separation Δt between two successive frames (in reference to double frame acquisition mode) is varied inside the range 0.45–1.50 ms depending on the flow Re and Ka , corresponding to a fluid displacement at the interface of around 8–15 pixels. Depending on the forcing frequency, 500–1000 PLIF image pairs are collected successively at a frequency of 100 Hz in each experimental run. Sample PLIF images, along with their processed and binarized counterparts are presented in Fig. 2.

The frames in the top row (Fig. 2(a)) show two example film fluorescence images, corrected for perspective distortion in DaVis. Referring to the image on the left, close inspection of the solid–liquid and gas–liquid boundaries reveals the presence of reflections. In the case of the solid–liquid interface, secondary reflections originating from the glass surface in contact with the liquid blur the PLIF signal locally, while at the gas–liquid interface, the fluorescence emitted by the illuminated liquid volume is reflected on the interface and back to the camera. Generally, it is noted that the primary fluorescence signal has a significantly higher intensity than these reflections, resulting in no ambiguity concerning the location of the liquid domain boundaries. In a few cases (e.g. image on the right), the reflection intensity in a small, localized region above and ahead of a large wave appears to be higher compared to the rest of the image; an effect most probably attributed to local curvature effects and manifested by lensing of the PLIF light emitted by the liquid bulk. Measurements conducted at higher Ka reveal that the local reflection intensity is a function of the height difference between the wave and substrate region ahead of the wave, as well as the absolute wave film thickness. The image on the right is plagued by particularly strong out-of-plane reflections ahead of the wave crest, to the extent that the gas–liquid interface

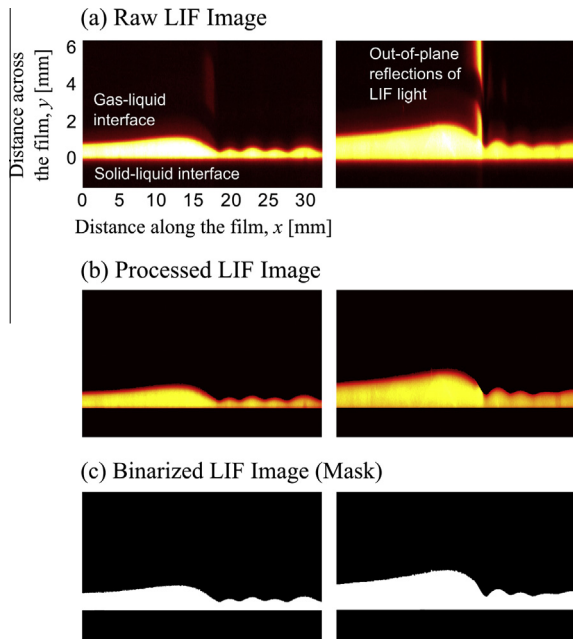


Fig. 2. (a) Refractive index and perspective distortion corrected PLIF images, (b) processed PLIF images in MATLAB whereby the solid-liquid and gas-liquid interfaces have been located and out-of-plane reflections have been removed, and (c) binarized PLIF image produced to mask out the liquid domain in the corresponding PIV image. The images presented in the first column from the left correspond to a flow with $Re = 63$ and $Ka = 350$, while those in the second column from the left, to a flow with $Re = 130$ and $Ka = 1800$.

is rendered locally indistinguishable. The procedure dedicated to the removal of the particular artefact will be discussed after the solid-liquid and gas-liquid interface identification methodologies have been introduced, which allow corrected images as in Fig. 2(b).

In systematically identifying the location of the two interfaces, different methods where devised and examined using in-house MATLAB-based processing routines. The location of the solid-liquid interface, for example, can be derived directly from the calibration performed with the graticule. This approach, however, assumes that the graticule attached to the calibration box is perfectly aligned with the illuminated solid-liquid boundary; if it is not, a systematic error will ensue. In order to minimize the possibility of manifestation of such an error, the correction box was attached to a micrometer stage allowing for precise positioning adjustments. The PLIF signal can also be used to obtain the location of the solid-liquid boundary, an approach adopted here through the implementation of an edge-detection algorithm. The particular

processing routine is typically employed in obtaining the Step Response Function (SRF) of an imaging system by use of the scanning edge technique Zhu et al. [50]. The signal level corresponding to the onset of the liquid domain is calibrated against the graticule, allowing for solid-liquid boundary identification directly from the experimental runs, thus also minimizing the possibility of a systematic error arising from the glass substrate bending under the weight of the film. With respect to the gas-liquid interface identification, an intensity threshold and two gradient methods were considered, and are presented by means of comparison in Fig. 3.

In the first case, the position of the interface y_{thresh} is obtained on a per image-column/pixel basis by setting a threshold intensity value I_{thresh} corresponding to a given fraction of the maximum PLIF signal:

$$y_{\text{thresh}} = \arg_y(I_{\text{LIF}}(y) - I_{\text{thresh}} = 0). \quad (4)$$

This is found to adequately account for the fact that the reflection intensity scales with the signal intensity; however, it fails to account for local lensing effects and consequently overestimates the film thickness where the interface is strongly curved.

In a second approach, the maximum (negative) gradient is used to estimate the location of the interface $y_{(I_{\text{LIF}}=0)}$ as the intercept of the maximum gradient line and the zero signal intensity axis:

$$y_{(I_{\text{LIF}}=0)} = y_{\text{max-grad}} \left(1 + \frac{I_{\text{LIF}}(y_{\text{max-grad}})}{\left(\frac{\partial I_{\text{LIF}}}{\partial y} (y_{\text{max-grad}}) \right)} \right), \quad (5)$$

where $y_{\text{max-grad}}$ is the y coordinate of the location of the maximum negative gradient:

$$y_{\text{max-grad}} = \arg_y \left(\max \left(-\frac{\partial I_{\text{LIF}}}{\partial y} \right) \right). \quad (6)$$

This approach, presented in Fig. 3(b), is found to be more robust than the threshold method as it remains largely unaffected by locally higher reflection intensities.

Finally, a third methodology incorporating elements from the previous two has been developed, whereby the location of the interface $y_{(I_{\text{max-grad}}=I_{\text{ref}})}$ is estimated as the intercept between the maximum PLIF signal gradient line $I_{\text{max-grad}}(y)$, and a line derived by fitting a first order polynomial to the reflection intensity profile $I_{\text{ref}}(y)$ (Fig. 3(c)). In more detail, beginning from the peak PLIF signal intensity on a per image-column/pixel basis, the reflection originating signal onset is taken as the first non-negative gradient location. The signal intensities of the following 30 pixels are then stored, averaged on a per image basis, and employed in producing the reflection line:

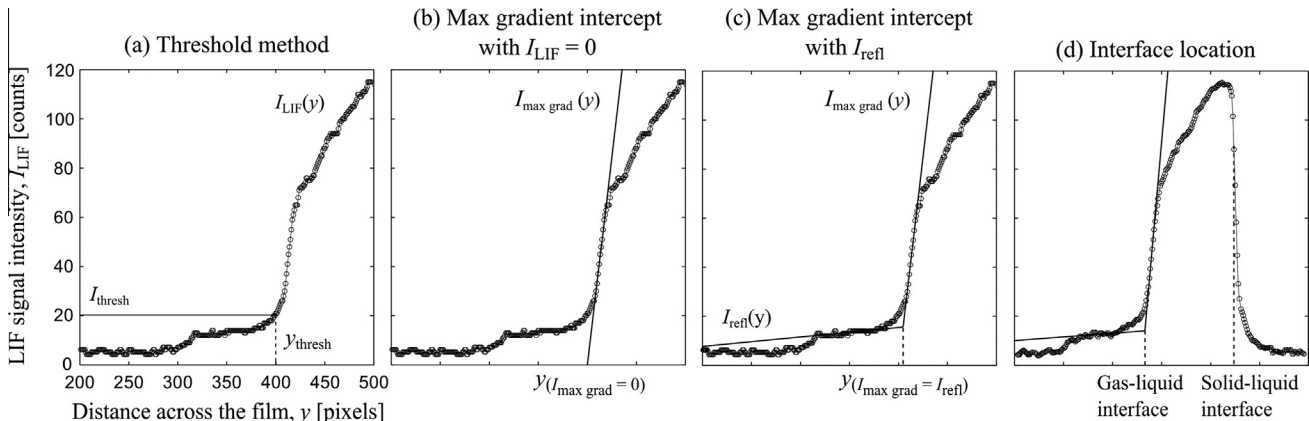


Fig. 3. PLIF intensity profile across the liquid domain demonstrating: (a) intensity threshold methodology for locating the gas-liquid interface, (b) maximum gradient intercept with the $I_{\text{LIF}} = 0$ line method, (c) maximum gradient intercept with the reflection first order polynomial fit approach, and (d) location of both interfaces.

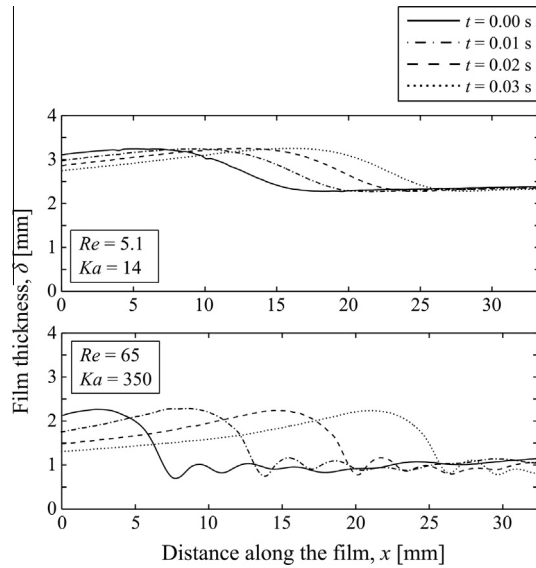


Fig. 4. Film thickness profiles of waves propagating along the direction of the flow extracted from successive PLIF images and corresponding to $Re = 5.1$ and $Ka = 14$ (top), and $Re = 65$ and $Ka = 350$ (bottom). In the second case, the profiles are corrected for out-of-plane reflections using interpolation.

$$y_{(I_{\max\text{grad}}=I_{\text{refl}})} = \arg_y(I_{\max\text{-grad}}(y) - I_{\text{refl}}(y) = 0). \quad (7)$$

The collected reflection data points are also averaged on a per column basis providing an indication of the reflection intensity profile along each image, with a local spike typically identified in regions where the wavy interface causes lensing. Compared to the maximum gradient method, the reflection intercept method produces smoother film-thickness results, while the gas–liquid interface location estimates are always closer to the initial signal increase, which is believed to be a more accurate estimate of the gas–liquid interface position. The effectiveness of the last method, in conjunction with the solid–liquid interface location approach in estimating the film thickness, is examined in Section 4.1.

Sample film thickness profiles extracted from successive PLIF images using the third interface identification method are displayed in Fig. 4 for $Re = 5.1$, $Ka = 14$ (top) and $Re = 65$, $Ka = 350$ (bottom). In a final processing step, the thickness traces were subjected to 3×3 median filtering to minimize signal noise while preserving the key signal features. The processed thickness profiles were then used to mask out the PLIF image regions not corresponding to film fluorescence, such as the reflection regions (Fig. 2(b)), and to produce binarized images (Fig. 2(c)) where a signal intensity of unity corresponds to a liquid film region and signal intensity of zero is ascribed to the rest of the imaged domain. The binarized PLIF images are also subsequently employed in correcting the corresponding PIV images for out-of-plane reflected particles, as discussed in Section 3.2.

With respect to frames bearing the artefact noted earlier (Fig. 2, right), the identification of the gas–liquid interface is conducted in two steps. Firstly, the procedure described above is implemented, resulting in a “spike” in the film thickness measurement at the wave front location. This spike is then identified by an algorithm that traces the local gradient of the thickness profile from both directions (left-to-right and right-to-left) and, consequently, removes the erroneous film thickness values that lie in between. These are subsequently replaced by interpolation using a smoothing spline. Sample film thickness profiles that have been treated in this manner are presented in Fig. 4 ($Re = 65$, $Ka = 350$).

In performing the aforementioned out-of-plane reflection correction, it is essential to examine the effect of the smoothing

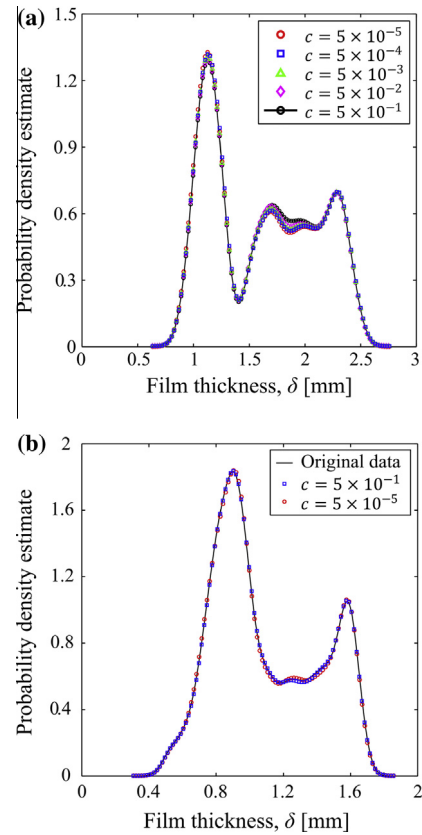


Fig. 5. (a) Film thickness probability density functions estimated using film thickness data from 200 PLIF frames containing large amplitude waves and out-of-plane reflections, and processed using different smoothing factors. (b) Film thickness probability density functions estimated using film thickness data from 50 PLIF frames containing lower amplitude waves and no and out-of-plane reflections, processed using different smoothing factors, and compared to the distribution obtained using the original data (right).

parameter c that was employed for this procedure. This smoothing parameter determines the trade-off between the roughness of the fit and the disparity between the fit and the original data. A parameter of value equal to zero generates a least-squares straight-line fit (essentially a linear polynomial fit), while a value equal to unity produces a piecewise cubic polynomial fit that passes through all the data points, and is referred to as a cubic spline interpolant. The effect of selecting an appropriate smoothing factor was examined by conducting two experiments.

In the first experiment, 200 pre-selected PLIF frames, all of which included waves with strong reflections at the wave fronts, were corrected using smoothing factors ranging from $c = 0.5$ to $c = 5 \times 10^{-5}$. The extracted film thickness data were then employed in estimating film thickness probability density functions using the non-parametric kernel density estimation approach. Upon comparing the resulting distributions (Fig. 5(a)), as well as the mean thickness values and standard deviations, the sensitivity of the correction methodology to the smoothing factor was evaluated. Varying the smoothing factor by as much as five orders of magnitude results only in slight local alterations in the film thickness probability density estimate. The disparity between the mean film thicknesses calculated for the two extreme smoothing factor values was below 1%. The effect of the correction methodology in the case of real experimental runs, in which only a select number of images include large amplitude waves is, therefore, expected to be even more limited.

The second experiment was designed to assess the absolute error associated with the fitting procedure. In this case, 50

pre-selected PLIF images containing large-amplitude waves that did not include strong reflections at the wave fronts owing to the overall lower film thickness and locally shallower gradients, were processed twice: (i) with the standard processing routine described previously; and then (ii) with the wave fronts manually removed and subsequently interpolated using the developed approach with $c = 0.5$ and $c = 5 \times 10^{-5}$. The resulting probability density distribution estimates resulting from this attempt, along with that of the original data, are shown in Fig. 5(b).

As the particular flow conditions are selected here so that no reflection was produced, the observed gradients ahead of the wave crests are lower than in cases where the implementation of the correction technique would be necessitated, resulting to a lower bound for the anticipated error. The latter, however, is limited to below 0.5% of the mean film thickness value for both examined smoothing factors, with the value $c = 0.5$ producing the better agreement, reproducing the standard deviation of the entire data set to within 1%. This particular smoothing factor value is therefore adopted in correcting film thickness profiles during post-processing of the actual experimental runs.

3.2. PIV data acquisition and processing

Raw image-pairs are collected by the PIV camera simultaneously with the PLIF camera (see Section 3.1), i.e., with an interframe separation in the range 0.45–1.5 ms depending on flow conditions, resulting in particle displacements near the interface of around 8–15 pixels. A sample raw PIV image, following corrections for refractive index and perspective distortion, is displayed in Fig. 6(a). In addition to the laser light scattered from the particles and the weak background fluorescence signal from the dye in the bulk of the liquid phase, two artefacts are also clearly discernible: (i) a reflection from the lower glass surface; and (ii) a reflection of the particle scattering signal of the entire illuminated volume about the gas–liquid interface/free-surface. It should be noted that similar to the reflection observed on top of the liquid film in the PLIF images, this reflection also follows the waviness of the gas–liquid interface. In contrast to the fluorescence signal reflection, however, the intensity of the reflected scattering signal is comparable to the original signal, rendering the identification of secondary scattering from the PIV images alone highly non-trivial. Nevertheless, it also should be added that there exists a significant discrepancy, in terms of the extent of the spatial regions occupied, on the one hand, by the direct and reflected (above the liquid free-surface) PLIF signals, and on the other, the equivalent regions in corresponding PIV images, which renders the presence of the PIV secondary scattered signals easily detectable even in raw unprocessed images.

In order to examine this particular effect and demonstrate that the particle scattering signal is indeed reflected about the interface, separate particle-imaging experiments were conducted using Rhodamine-B-doped PIV particles (LaVision, 10- μm mean diameter). The reason for selecting the specific particles for the purposes of this experiment is that they can be imaged with both PLIF and PIV cameras, as part of the incident laser light is absorbed and re-emitted as red-shifted fluorescence, and part of it is scattered. Sample PLIF and PIV images of a particle pair collected successively at 0.02 s intervals, from these imaging experiments, are shown in Fig. 7. Particle 1 is located very near the interface, while Particle 2 is suspended approximately halfway across the film height and further downstream along the direction of the flow (PLIF frame at $t = 0.00$ s). The same particle pair imaged simultaneously with the PIV camera appears twice, with Particle 1 observed as a double particle and Particle 2 mirrored about the interface. The next two PLIF–PIV frames capture the same particle pair at $t = 0.02$ s and $t = 0.04$ s, with Particle 1 overtaking Particle 2 along

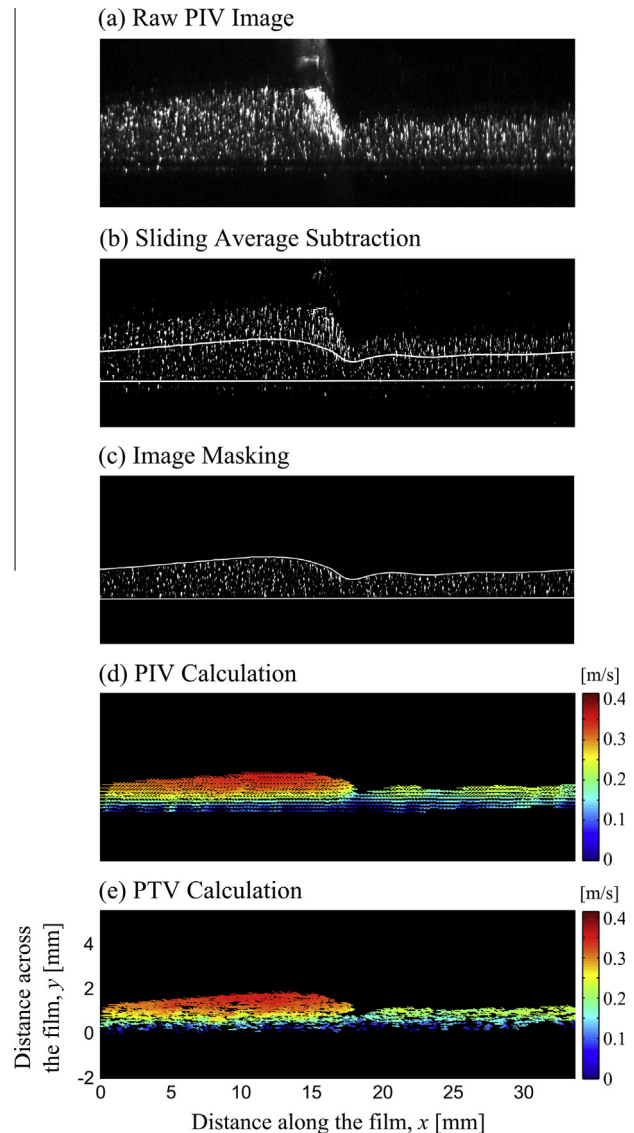


Fig. 6. (a) Refractive index and perspective distortion corrected particle image, (b) the same image following sliding average subtraction, (c) masked particle image using its processed PLIF counterpart, (d) PIV velocity vector map obtained from a masked image pair such as the one shown above, and (e) PTV velocity vector map obtained following the PIV calculation.

the direction of the flow as a result of the higher velocity at the interface compared to the liquid bulk.

Returning to the PIV/PTV image acquisition and processing, once an experimental run has been completed, the sequence of collected frame pairs is processed using DaVis PIV/PTV algorithms. Specifically, following corrections for refractive index and perspective distortion, the collected images are preprocessed using a sliding-average subtraction to suppress any background signal originating from Rhodamine fluorescence and reflections, improving signal-to-noise (Fig. 6(b)). The binarized images generated by the PLIF image processing routine in MATLAB are then imported into DaVis and employed to mask out regions associated with reflections from both the glass substrate and the gas–liquid interface (Fig. 6(c)). This avoids the computation of vectors below the solid–liquid and above the gas–liquid interface; normally vectors will be computed in such regions as the interrogation windows will partially be occupied by particles that lie within the masked boundaries Kähler et al. [51]. In the masking procedure, vectors are disabled if they are found to originate from interrogation windows that have a masked-out

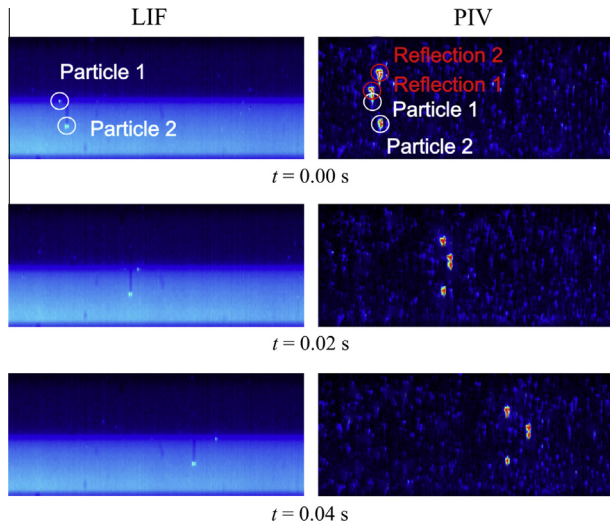


Fig. 7. Rhodamine B particle pair imaged at three successive time instances using two cameras; one equipped with a long-pass PLIF filter and one equipped with a band-pass PIV filter. In the case of the PIV imaging setup, the particle pair is observed twice; once as a real image corresponding to the one observed with the PLIF setup, and then as a mirror image due to reflection about the interface.

area as a fraction of the entire interrogation window higher than 0.2 for the first pass and 0.5 for all other passes.

In a next step, the masked particle images are used to generate two-dimensional velocity vector maps using a four-pass cross-correlation approach. For the first and second passes, a 32×32 pixel interrogation window is selected with the overlap parameter set to 50%. For the third and fourth passes, the interrogation window is reduced to 16×16 pixels with 50% overlap. The resulting PIV vector-to-vector spatial resolution is estimated as being between $222.4 \mu\text{m}$ and $236.6 \mu\text{m}$, depending on the experimental round (liquid composition). The following processing steps are applied to intermediate velocity vector-maps generated during the initial passes: (i) a cross-correlation detectability filter removes vectors if the peak cross-correlation ratio is lower than 1.5; (ii) a median filter deletes vectors with values exceeding the median of their neighbours by more than 1.5 times the RMS value of the latter, and re-inserts them if the median value is exceeded by more than 2.5 times the RMS value; (iii) a vector density filter removes groups containing less than 8 vectors; (iv) an interpolation/extrapolation routine fills empty regions; and (v) a 3×3 smoothing filter is used for denoising. Similar post-processing steps are utilized for the final pass results: (i) spurious vectors (vectors having a norm or direction significantly disparate compared to their neighbours) are removed by applying allowable vector range restrictions ($-0.25 \leq U_x \leq 1.5$ and $-0.25 \leq U_y \leq 0.25$); (ii) a cross-correlation detectability filter is used with the peak cross-correlation ratio threshold set to 1.25; and (iii) vector density and median filters are applied, as before. A sample PIV velocity vector map resulting from this procedure is presented in Fig. 6(d).

Individual particles are subsequently tracked (PTV calculation) by employing the obtained PIV results as reference estimators of the velocity field, and the following PTV calculation parameters and features: (i) a 1–5 pixel allowable particle-size range is implemented in order to account for the effects of dewarping and collection optics point spread function on the apparent image size of the particles (typically in the 2–4 pixels range); (ii) an intensity threshold is applied that distinguishes individual particles from background noise; (iii) an 8×8 pixel window is selected for particle correlation; and (iv) ± 2 pixel allowable vector range relative the reference PIV data is imposed. Finally, a median filter is applied, in

the same manner as for the PIV post-processing. The resulting PTV vector field corresponding to the illustrated PIV image in Fig. 6(d) is presented at the final frame of the same figure, Fig. 6(e).

Once the PIV and/or PTV velocity vector maps are generated, instantaneous velocity profiles from within the wavy films can be constructed, such as those in Fig. 8. (The film thickness profile displayed in this figure is obtained from the PLIF processing routine described in the previous section, Section 3.1.) Instantaneous and local velocity profiles can then be recovered by averaging PIV and PTV data over small regions at different positions in the streamwise (x) direction (e.g., 4 such positions are indicated in Fig. 8). For the PIV profiles, spatial averaging is carried out over 5 PIV windows (each one corresponding to 8 pixels) around each position, while for the PTV profiles, the same spatial region (1.143 mm) is used for averaging, which is now represented by 40 pixels.

A number of remarks can be made concerning the application of PIV and PTV for velocity-field measurements in the present film flow experiments. First, PTV provides an eight-fold increase in spatial resolution (not measurement resolution) compared to PIV given the employed calculation settings, optical setup and particle selection. When extracting velocity profiles, however, this resolution advantage applies only to the direction perpendicular to the flow (cross-stream direction), since the profiles are obtained by using a spatial average over the same physical domain in the streamwise direction. Beyond its reduced spatial resolution, PIV is also known to suffer from significant bias errors in the presence of strong shear (velocity gradients), as the particle group motion is averaged within the interrogation window. The ensuing systematic errors are exacerbated in the near-wall region, where the particle image displacement diminishes; for constant spatial resolution, interframe separation (time interval between successive illuminations) and precision in the correlation peak estimation, the relative uncertainty in the velocity measurement increases in this region. This effect is clearly observable in the PIV profiles presented in Fig. 8, where velocity vectors at the wall always exhibit positive displacements, while the immediately adjacent ones, centred 0.229 mm away from the wall in this case, also display a bias towards higher velocity values. In contrast, data derived by employment of PTV show significantly lower velocities in the same region. Away from the wall, data obtained by either measurement method are in good agreement, as expected. These observations are aligned with conclusions stemming from the meticulous analytical and experimental efforts of Kähler et al. ([52,51]). Finally, the presence of particle image reflections (from either liquid-domain interface) inside the masked liquid domain constitutes another source of error, this time affecting both PIV and PTV velocity results. In the case of the former, this effect is indistinguishable from any bias originating from the employment of a window-based correlation approach in the near-wall region, while for the latter it manifests as a bias towards higher velocities when time-averaging or space averaging over larger domains. Uncertainties that affect near-wall velocity measurements and are attributed to optical phenomena are commonly encountered in the literature, for example Kähler et al. [53], and may, depending on the experimental setup, be unavoidable. With reference to the present measurement campaign, the effect of reflections on the near-wall PTV data and the limitations they impose will be discussed explicitly in the results section (specifically, the text that discusses Fig. 13).

3.3. Fluid property determination

The surface tension, viscosity and density of the four aqueous glycerol solutions employed in the current investigation were determined experimentally. The glycerol concentrations were 82% (Solution 1), 65% (Solution 2), 45% (Solution 3) and 21% (Solution

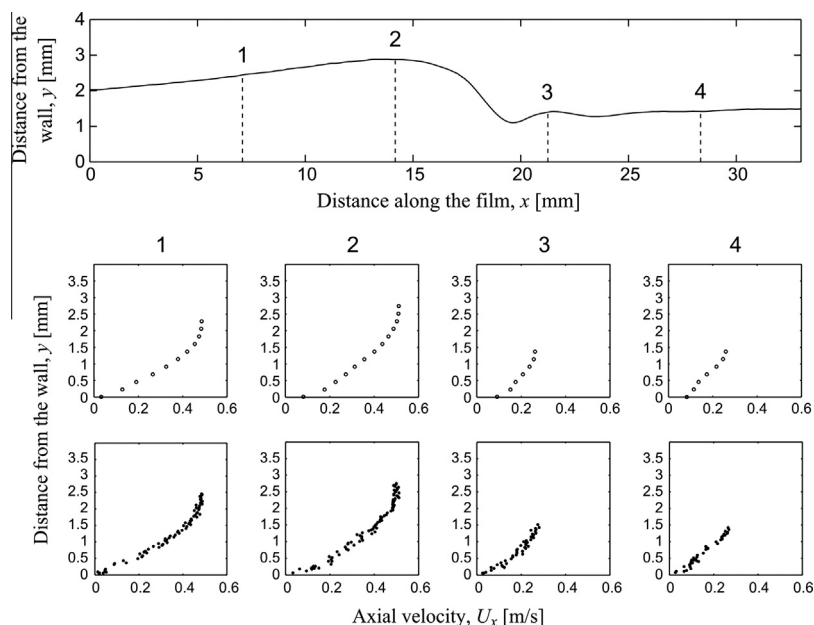


Fig. 8. Instantaneous velocity profiles produced by spatially averaging PIV (top plots) and PTV (bottom plots) velocity data at four locations along the corresponding, PLIF-derived instantaneous film thickness profile ($Re = 26$, $Ka = 85$).

4) by weight. An Attension Sigma 700 force tensiometer equipped with a Wilhelmy plate was used to quantify the surface tension of samples collected throughout the duration of optical measurement runs. This was done in order to examine whether surface tension variations would ensue over time due to the solution exposure to the laboratory environment, and the possible deposition of dust particles acting as surfactants. Once a sample was placed in the tensiometer, it was heated to the desired temperature (corresponding to the optical experiments) before a measurement was collected. Five independent measurements (samples) were conducted for each solution, and uncertainties were calculated based on the standard deviation thereof. No systematic variation was observed among samples collected throughout the duration of the same optical measurement run. In order to verify the validity of the measurement procedure, the surface tension values of deionized water and pure glycerol were also measured, whereby very close agreement with literature values was observed. The aforementioned disparity is therefore most likely attributed to the presence of PIV particles as well as other surfactants such as dust and even the Rhodamine dye, known to reduce the surface tension of water-rich solutions. For the viscosity measurements, four Poulten Selfe & Lee U-tube viscometers were employed depending on the relative glycerol content of

each solution, while the densities of the four aqueous glycerol solutions were determined using an electronic scale and a 1 L beaker.

The measured surface tension, kinematic viscosity and density were used to calculate the flow Re and Ka . All three properties are provided in Table 1, along with their respective percentage relative uncertainties. The quoted uncertainties in the viscosity and density results were calculated in the same manner as the surface tension ones. Along with the aforementioned properties, the range of measured liquid flow-rates (ultrasonic flowmeter measurements), and calculated Re and Ka pertaining to the current experimental campaign are also tabulated. The uncertainty associated with the flowmeter measurement is given as quoted by the manufacturer for the respective flow-rate range. For the two dimensionless numbers, standard error values are stated.

4. Results and discussion

4.1. Validation and quality assurance experiments

Film thickness measurements using the aforementioned PLIF setup were carried out for flat (unforced and viscous) films, and the results were compared to measurements carried out using a

Table 1
Experimentally determined kinematic viscosity ν_f , surface tension σ_f and density ρ_f values of the four aqueous glycerol solutions employed in the presently described experimental campaign, presented along with their respective percentage relative errors and the resulting ranges of Re and Ka . The uncertainties of the two dimensionless numbers obtained using the aforementioned liquid properties and liquid flow-rates Q_L , are also tabulated alongside the latter.

Liquid	$\nu_f \cdot 10^6 (\text{m}^2/\text{s})$	$\sigma_f \cdot 10^3 (\text{N/m})$	$\rho_f (\text{N/m})$	$Q_L \cdot 10^5 (\text{m}^3/\text{s})$	Re	Ka
Solution 1 ($T = 25.0^\circ\text{C}$)	$61.7 \pm 2.1\%$	$62.3 \pm 2.8\%$	$1214 \pm 0.15\%$	4.1–10.3 $\pm 3.0\%$	2.3–5.8 $\pm 3.7\%$	$14 \pm 4.0\%$
Solution 1 ($T = 28.0^\circ\text{C}$)	$51.4 \pm 1.9\%$	$61.8 \pm 1.0\%$	$1214 \pm 0.15\%$	9.0–10.7 $\pm 3.0\%$	6.1–7.3 $\pm 3.6\%$	$18 \pm 2.7\%$
Solution 1 ($T = 30.0^\circ\text{C}$)	$46.0 \pm 1.6\%$	$60.6 \pm 1.1\%$	$1214 \pm 0.15\%$	9.8–11.3 $\pm 3.0\%$	7.4–8.5 $\pm 3.4\%$	$20 \pm 2.4\%$
Solution 2 ($T = 25.5^\circ\text{C}$)	$15.8 \pm 3.2\%$	$58.7 \pm 1.1\%$	$1169 \pm 0.11\%$	3.3–14.0 $\pm 3.0\%$	7.4–31 $\pm 4.4\%$	$85 \pm 4.4\%$
Solution 3 ($T = 25.2^\circ\text{C}$)	$5.77 \pm 1.6\%$	$59.7 \pm 3.6\%$	$1113 \pm 0.12\%$	1.5–12.9 $\pm 3.0\%$	9.3–78 $\pm 3.4\%$	$350 \pm 4.3\%$
Solution 4 ($T = 25.4^\circ\text{C}$)	$1.71 \pm 0.6\%$	$58.1 \pm 1.2\%$	$1054 \pm 0.09\%$	3.5–15.6 $\pm 3.0\%$	71–320 $\pm 3.1\%$	$1800 \pm 1.4\%$

micrometer stage (10 μm smallest scale division). The objective of this particular set of experiments was to obtain an independent film thickness measurement that could allow for the identification of potential systematic and random errors in the PLIF measurement method. More than 20 different flow conditions spanning film thicknesses in the 1–3 mm range were tested in two sets of runs.

Initially, 25 images of the calibration target immersed in Solution 1 (Table 1) were collected, averaged, and used for optical distortion corrections in same manner discussed earlier in Section 2.3 (Fig. 1(c)). A micrometer was then placed on top of the imaging region and a reading of the solid substrate location was obtained. Following this, a set of 11 films of different thicknesses were generated (Run 1) by varying the power input to the pump and adjusting the portion of the flow bypassing the test section (Fig. 1(a), Valve V4). For each flow setting, 200 PLIF images were collected and processed in order to evaluate average and standard deviation film thickness data, while a second reading of the film surface height at each flow setting was made using the micrometer. Film thickness statistics were generated by randomly selecting 5 film thickness data points from each image without replacement. After this set of experiments (Run 1) was completed, a second substrate location measurement was carried out, and the two values, prior to and at the end of the run, were averaged. This practice was adopted in order to verify that the micrometer was not displaced during the set of experiments. The disparity between the initial and final wall location measurements did not exceed 20 μm . At this point, a second set of experiments (Run 2) was carried out by repeating the entire procedure (PLIF camera and micrometer calibrations). The film thickness data collected using the two techniques are plotted against each other in Fig. 9.

Inspection of the data presented in Fig. 9 reveals no systematic error; the disparity between the micrometer and PLIF-derived film thicknesses never exceeds 100 μm , while the average and RMS absolute deviations between the two measurement methods are below 10 μm and 30 μm respectively. On a relative basis, this amounts to no more than 1% and 3% of the thinnest film of the examined range. Errors introduced into the PLIF measurement are linked to the employed optical arrangement, as the practice of illuminating from the liquid below the glass plate and dewarping to correct for the refractive index mismatch affects the sensitivity of the gradient method in detecting the gas–liquid interface. The alleviation of the need for the optical correction by choosing matched refractive indices for the substrate and liquid, as noted earlier, would most probably be more effective in this particular aspect of the technique. However, such practice would impose severe limitations to fluid selection and our ability to vary Ka , which is

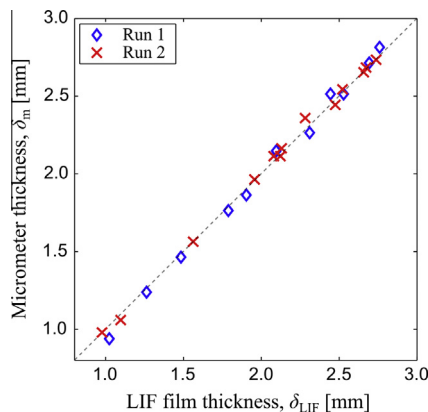


Fig. 9. Film thickness measurements of flat films ($Ka \sim 14$) carried out using a micrometer and plotted against PLIF measurements carried out alongside the former for two independent measurement runs.

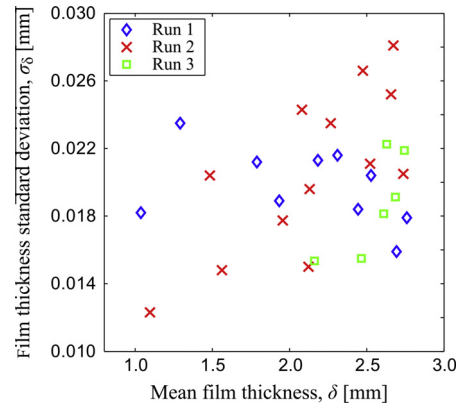


Fig. 10. Quantification of the PLIF-based film thickness measurement noise as the film thickness standard deviation observed in flat films. Data from the two runs presented in Fig. 9 were reproduced and plotted along with flat-film experiments carried out simultaneously with PTV measurements.

of importance for the purposes of the present experimental campaign.

An estimate of the PLIF-derived film thickness measurement error, stemming from camera noise (and also to some extent by natural film thickness variations), can be obtained by inspection of the film thickness standard deviation data plotted in Fig. 10 as a function of the mean film thickness. The supplementary data points (Run 3) correspond to 1000 images each carried out along with simultaneous PTV measurements in a similar set of flat-film flows. The film thickness standard deviation for all plotted data points is slightly lower than the apparent spatial resolution (29.57 $\mu\text{m}/\text{pixel}$).

In addition to comparisons between PLIF-derived film thickness measurements and micrometer stage measurements, the mean film thickness, interfacial velocity and bulk flow velocities of six flat films spanning three Ka (14–20), were compared to the one-dimensional (1-D), steady, fully developed gravity-driven film flow solution of the Navier–Stokes equation, also referred to as the Nusselt solution (Nusselt [54]). The film thickness d_{film} prediction is expressed in Eq. (9) as a function of the fluid kinematic viscosity ν_f , the flow Re , the gravitational acceleration g and the inclination angle θ , while the interfacial velocity U_d along the streamwise direction of the flow can be calculated from Eq. (11) by setting $y = \delta$ (y being the coordinate perpendicular to the wall). The resulting expression is provided in Eq. (12). The expression in Eq. (10) is obtained by substituting Re in Eq. (9) with the expression provided in Eq. (3), where Q stands for the volumetric flow-rate and w for the width of the channel (and distribution box). Finally, the film bulk velocity U_b is obtained by integrating the velocity profile across the film thickness (from $y = 0$ to $y = \delta$). The analytical expression (Eq. (13)) shows that the bulk velocity amounts to 2/3 of the interfacial velocity value.

$$\delta = \left(\frac{3\nu_f^2 Re}{g \sin \theta} \right)^{\frac{1}{3}} \quad (9)$$

$$\delta = \left(\frac{3\nu_f Q}{g w \sin \theta} \right)^{\frac{1}{3}} \quad (10)$$

$$U_y = \frac{g \sin \theta}{\nu_f} y \left(\delta - \frac{y}{2} \right) \quad (11)$$

$$U_d = \frac{g \sin \theta \delta^2}{2\nu_f} \quad (12)$$

$$U_b = \frac{g \sin \theta \delta^2}{3\nu_f} \quad (13)$$

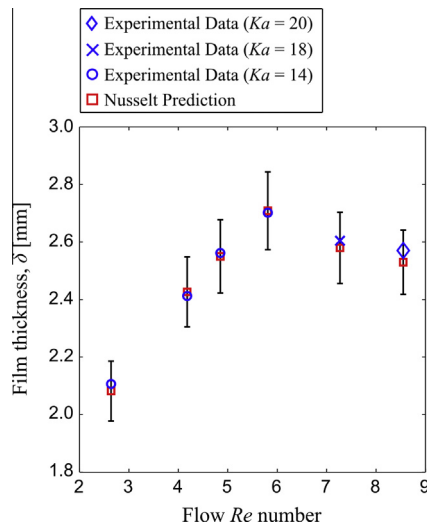


Fig. 11. Average flat-film thickness data obtained from PLIF experiments and plotted against calculated film thickness values for six different flow conditions using Eqs. (9) and (10). The error bars were generated by considering all experimental error sources associated with the analytical calculation.

We proceed now to compare, in Fig. 11, film thickness data derived from PLIF and film thicknesses calculated using Eqs. (9) or (10). Some variables used in these particular expressions are associated with measurement uncertainty and therefore, an error analysis was performed. The error bars on the points corresponding to the analytically derived film thickness values indicate the average errors calculated. Compared to the standard error, the average error typically generates higher values, and can thus be employed as an “upper bound” error estimator. The results in Fig. 11 suggest that the experimentally derived film thicknesses are in excellent agreement with expectations from the theory, over the entire range of Ka tested. The mean absolute deviation between the experimental and analytically derived values is $23\ \mu\text{m}$, with the mean relative deviation being 0.9% . Worst-case deviations range from 1.3% to 1.9% for the lowest and highest Ka respectively, with the intermediate Ka flow error amounting to 1.2% .

Comparisons were also made between analytically derived predictions of the interfacial and bulk velocities (Eqs. (12) and (13)), and values obtained from processed PTV data for the purpose of validating the latter. Since the δ values employed in the analytical velocity expressions were derived from PLIF measurements, the film thickness measurement error used in calculating both interfacial and bulk velocity errors was taken as the mean deviation between the measured and analytically derived film thicknesses ($23\ \mu\text{m}$). The mean relative deviation between the two interfacial velocities amounts to 3.2% , with worst-case error values of approximately 5.3% . Bulk velocities were evaluated by integrating time-averaged axial velocity profiles across the film thickness using the trapezoidal rule. PTV rather than PIV velocity data were employed so as to avoid the typical inaccuracies associated with PIV measurements in film flows, as discussed previously (Section 3.2). The same mean relative deviation was observed (3.2%), while the maximum error was 4.5% . Both interfacial and bulk velocity data fit within the range of velocity values defined by the error bars.

Axial velocity profiles are presented for $Ka = 14$ and $Re = 5.8, 4.9$ and 2.6 , and compared to corresponding analytically derived profiles in Fig. 13. The horizontal error bars represent the standard deviation of velocity at each depth inside the film where a PTV calculation was carried out, and serve as local quantifiers of random errors. The following remarks can be made:

- (i) For all three examined flows, excellent agreement between the measured and analytically derived profiles is observed. As a consequence, a similarly exceptional agreement would be expected for these flow conditions in the data plotted in Fig. 12.
- (ii) As discussed earlier, both PTV and PIV near-wall measurements are affected by local reflections, which give rise to locally higher than anticipated velocity components. In the presently examined flows, this phenomenon affects regions of approximately $100\text{--}200\ \mu\text{m}$ away from the solid–liquid interface, a spatial extent corresponding to about $5\text{--}7\%$ of the examined flow fields.
- (iii) Local velocity standard deviations are observed to decrease with increasing distance from the wall; at the gas–liquid interface, they typically amount to less than 1% of the mean value, while halfway across the film thickness, to approximately 6% .

The final comparative study is aimed at validating combined PLIF–PTV results against flow rate measurements carried out using the ultrasonic flowmeter (Fig. 14). Continuity dictates that the flow rate in the distribution box (ultrasonic flowmeter measurement) should equal the mean flow rate over the plate. The latter can be obtained by obtaining flow rates based on the film bulk velocity (PTV) and the film thickness (PLIF), assuming any three-dimensionality effects are negligible. This calculation was performed by averaging out film thickness data along a $1.8\ \text{mm}$ region of the flow on a per image basis, while for the PTV data, a space-averaged axial velocity profile was generated over the same spatial domain, and subsequently integrated. Thus, every PLIF–PTV image pair contributed a single instantaneous flow-rate measurement. Upon averaging these flow-rate values over the entire data set a mean flow-rate was obtained. Apart from the six flat-film flows employed in the previous validation exercises, data sets from harmonically excited films covering all four Ka fluids were also considered in conducting this comparative study.

Fig. 14 shows flow-rate data from the combined PLIF–PTV optical technique plotted against direct flow-rate measurements from the flowmeter (top plot), and flow-rate data recovered by both methods (i.e. flowmeter measurements and combined PLIF–PTV results) plotted as a function of the flow Re (bottom plot). The latter is calculated using Eq. (3) and the flowmeter measurement. It should also be noted that results pertaining to all four Ka number film flow experiments have been included, in order to examine whether the more complex topology of the thinner films observed

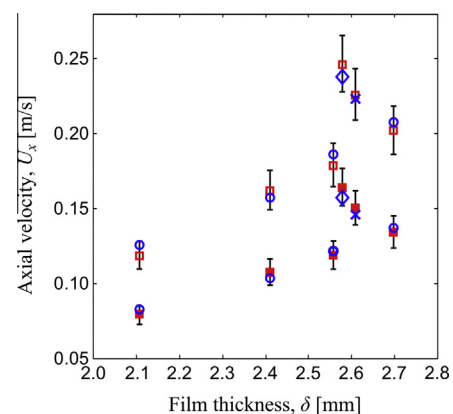


Fig. 12. Mean interfacial and bulk velocities obtained from time-averaged PTV measurements, plotted along with analytically derived data against measured film thickness values. The same flow conditions and annotations thereof apply to this figure as in Fig. 11. Bulk velocities are signified by solid, rather than empty markers.

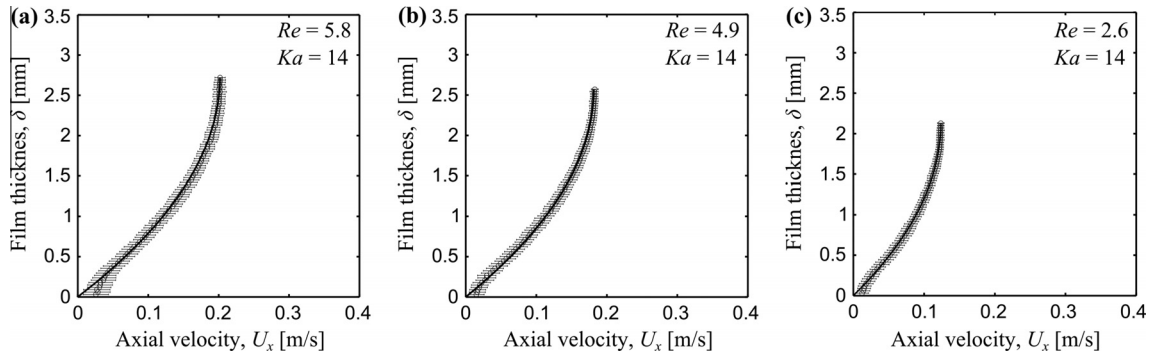


Fig. 13. PTV derived axial velocity profiles plotted along with their analytically derived counterparts (solid lines) using Eqs. (10). Horizontal error bars represent PTV-derived local standard deviations. The presented data originate from the same experimental measurements used for generating Fig. 12: (a) $Re = 5.8$, $Ka = 14$, (b) $Re = 4.9$, $Ka = 14$, and (c) $Re = 2.6$, $Ka = 14$.

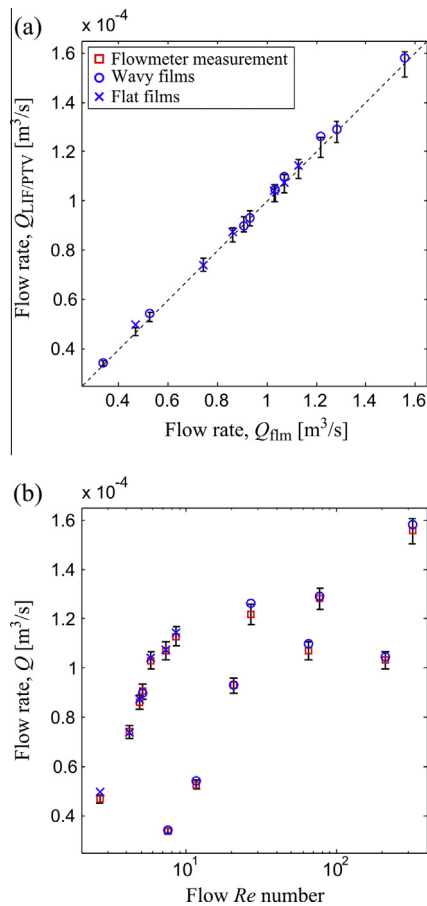


Fig. 14. Mean flow-rate measurements recovered using PTV-derived bulk velocity data and PLIF-derived film thickness data, plotted against: (a) corresponding ultrasonic flowmeter measurements, and (b) corresponding Re (approximately spanning the range $Re = 5$ –320). The error bars represent the uncertainty associated with the flowmeter measurement (3% of reading).

at higher Re and Ka numbers affect the effectiveness of the optical technique in retrieving flow-rate data. The results suggest that no systematic trend exists in the observed deviations. The majority of the results derived from the optical data lie within the flow rate range of values defined by the error bars, which represent the uncertainty associated with the flowmeter measurement (3% of reading). The mean relative deviation corresponds to 1.6%, the RMS value to 2% and the maximum to 6%.

No extensive comparative studies were attempted for the quantitative uncertainty assessment of PIV-based measurements, on

account of the inherent weaknesses involved in the application of the particular technique compared to PTV in these flows. It is, however, our experience that PIV measurements can comfortably serve qualitative assessment purposes, while also being capable of producing accurate velocity data away from the wall. This was validated by comparing PIV with PTV data, with mean velocity values not deviating by more than 5%. Two important parameters associated with the PIV calculation error, ignoring for the moment the previously noted (Section 3.2) shortcomings, are the particle density within the set interrogation window, and the particle image displacement. The latter can be moderated by adjusting the interframe separation, which as noted earlier was varied so as to allow for particle displacements of around 8–15 pixels at the interface. In order to obtain a quantitative estimate of the velocity errors in that region, an average particle density was obtained by employment of the ImageJ image processing software package for the 32×32 pixel interrogation window used in the first and second passes of the PIV vector calculation. This value corresponded to an average of 8.4 particles for the 50 selected images from the $Re = 5.8$ and $Ka = 14$ flow data set; Keane and Adrian [55,56] showed that the probability of valid displacement detection exceeds 95% for double-frame PIV when 5 particles are present within an interrogation window of that size.

4.2. Film topology and time-averaged axial velocity profiles

The purpose of this, as well as the following section, is to demonstrate key topological interfacial wave features, local time-averaged and moving frame-of-reference wave/phase-locked average velocity results obtained by the PLIF-PTV methodologies described earlier. The currently implemented post-processing calculations and corresponding results are by no means exhaustive; on the contrary, they are simply indicative of the breadth of information and insight that can be gained by employment of the proposed combined optical technique.

Firstly, temporal film thickness traces were constructed and are presented in Fig. 15 (left column), with emphasis placed on the shape of the interface when the inlet flow is subjected to different forcing frequencies. In these experiments, both Re and Ka were kept constant ($Re = 5.1$ – 5.2 and $Ka = 14$, respectively), while the forcing frequency was varied from 2 to 6 Hz (note the subsequent quasi-periodic nature of the resulting films). In generating these temporal traces, a single film thickness measure was extracted from each instantaneous spatial film thickness profile; in turn, every PLIF frame collected during a run contributed one such spatial profile. At the maximum recording rate achievable by the imaging system, 100 double frames were collected per second yielding 200 data points; data points belonging to the same frame

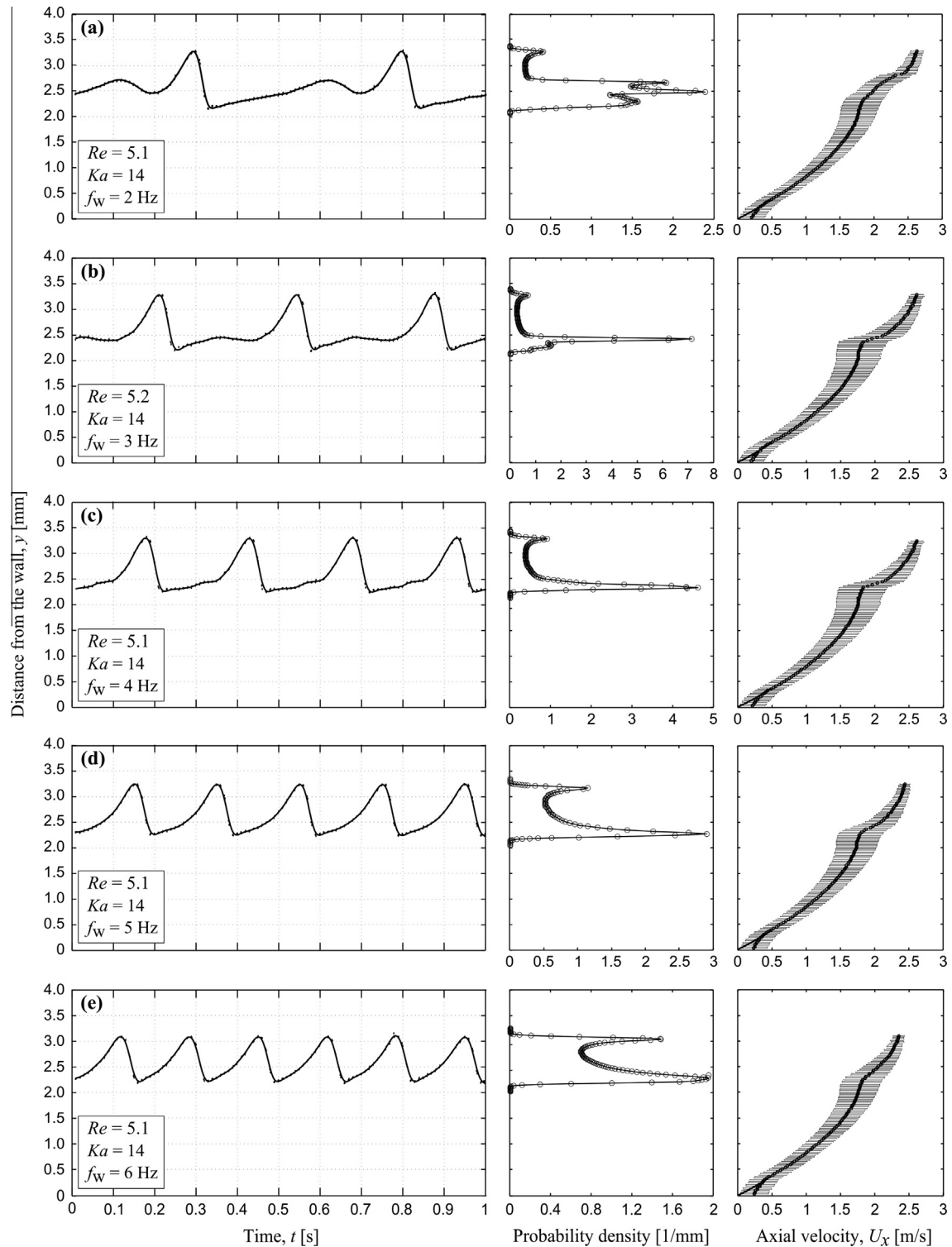


Fig. 15. Left: temporal film thickness traces generated by use of a single film thickness measurement point (pixel) from 100 double PLIF frames collected over the course of 1 s. From (a) to (e) (top to bottom) the forcing frequency increases by 1 Hz spanning the range 2–6 Hz. The flow Re ranges between 5.1 and 5.2, while Ka is constant and equal to 14. Middle: Film thickness probability density estimates obtained by sampling 50 data points from each image. Right: time-averaged, PTV-derived axial velocity profiles and velocity deviations around the time-averaged profiles as a function of film height (the error bars represent the standard deviation of local axial velocities).

pair were temporally separated by 1.5 ms, while data points originating from successive frame pairs were separated by 10 ms. In the plots in Fig. 15, a smoothing spline interpolation is shown along with the actual data points.

The frequency sweep can be used to demonstrate the transition from multi-peaked solitary waves to saturated sinusoid-like waveforms as the wave frequency increases past a critical phase

boundary (Liu et al. [16], Liu and Gollub [17]). In more detail, two different types of non-linear forced periodic wave evolution are identified:

- (i) At low frequencies, between 2 and 3 Hz, double-peaked waveforms are observed with higher amplitude solitary waves being trailed by broader and slower, as the PIV/PTV

measurements reveal, humps. Along the direction of the flow and nearer to the inlet, fast-moving waves grow selectively and absorb the secondary, slower moving instabilities further downstream; given enough distance from the inlet, the flow develops into spatiotemporal chaos. Presently, wave topology and PIV/PTV measurements were conducted at a single location (approximately 25 cm downstream of the distribution box), where these lagging secondary waves are still clearly discernible.

- (ii) At higher frequencies, between 4 and 5 Hz, the subsidiary waveforms disappear, and only fully developed single-peaked waves are encountered. When the wave frequency is increased to 6 Hz, the interface assumes a “saw tooth” pattern.

The observations regarding the presence of secondary spatial subharmonic instabilities at low forcing frequencies and their subsequent withdrawal with increasing wave frequency can also be verified by examining the film thickness statistics of these films, and in particular, the probability density functions of the film thickness distributions. In selecting film thickness data for the purpose of deriving statistical results, a compromise is typically required between statistical independence and statistical convergence. In estimating film thickness probability density functions, the non-parametric kernel density estimation approach was employed. The obtained probability density estimates are presented in the middle column of Fig. 15. The following deductions can be made:

- (i) At the lowest wave frequency (2 Hz) the film thickness probability density function displays four distinct peaks; one corresponding to the primary wave crests, one to the primary wave troughs, one to the secondary wave crests and one to the secondary wave troughs.
- (ii) Increasing the forcing frequency to 3 Hz results to the collapse of the last three maxima into a dominant peak and a weaker one, with the film thickness mode (2.46 mm) lying between the mean wave trough height (2.24 mm) and the flow mean height (2.57 mm).
- (iii) As the wave frequency increases from 4 Hz to 6 Hz, the estimated probability density functions develop a bimodal sinusoid-like shape.

Time-averaged axial velocity profiles were also generated by the employment of PTV (right column of Fig. 15), with the plots aligned and sharing a vertical axis with those of the film thickness time-traces and probability density functions. No normalization to the instantaneous velocity profiles was applied here (see for example Mudawar and Houpt [2], Moran et al. [40]), such that the velocity profiles were calculated based on velocity values at each absolute distance from the wall, given a presence of liquid within the interrogation window at those locations. Consequently, for a distance near the crest height value, velocity data were only available when liquid appeared in the wave crests, while for a distance corresponding to the wave trough height, data from the entire run were averaged. Along with average axial velocities, error bars corresponding to the standard deviation of the axial velocity data at all measurement locations have been added to the plot, in same manner as in Fig. 13. Here, however, the objective is to quantify axial velocity fluctuations rather than random errors associated with the measurement technique. Parabolic fits in the near-wall region are added in order to illustrate the regions where local velocity values are affected by reflections.

The following observations can be made based on the time-averaged axial velocity profiles and their relation to the supplementary interfacial topology results in the first two columns in Fig. 13:

- (i) Velocity data adjacent to the wall and up to a distance of around 200–250 μm away from it display the same bias that was observed earlier in the flat-film comparisons to calculated Nusselt profiles (Fig. 13). Therefore, the generation of locally erroneous values by PTV that stems from local particle reflections affects up to approximately 5–7% of the spatial extent of the film. It is noted, however, that in the case of very thin (sub-millimetric) films this error can be closer to 10%.
- (ii) Unlike the parabolic profiles observed in the study of flat films, the presently examined profiles exhibit different shapes depending on the forcing frequency. In more detail, for the 2 Hz forcing frequency flow (Fig. 15(a)), parabolic behaviour can be assigned to a substrate region, above which a transition to a second parabolic shape is observed. As the forcing frequency increases, the transition region gives way to the second parabolic profile. This behaviour stems from the presence of distinct flow fields below the wave crests and flat flow regions in low wave frequency laminar films; at sufficiently high forcing frequencies (past the 10 Hz limit imposed in this study) it may be speculated that a single parabolic profile will adequately fit the time-averaged velocity data. Similarly, if Re increases (especially past the purely laminar regime), the presently discussed effect is also expected to be less pronounced. Evidence in support of the second suggestion were found for $Ka = 1800$ and $Re = 290\text{--}320$, for forcing frequencies of 7 and 10 Hz.
- (iii) It is very interesting to note that the shape transitions in the time-averaged velocity profiles correlate strongly with the peaks of the probability densities. For the 3–6 Hz wave frequency cases, the film thickness modes coincide consistently with the transition film heights (or distances from the wall). In the 2 Hz flow, the transition region is bounded by three adjacent peaks, with the lowest film thickness one signifying the end of the parabolic profile representative of the substrate region and the highest film thickness one matching the onset of the second parabolic region.
- (iv) The shapes of the time-averaged velocity profiles have been shown to change in the vicinity of the film thickness modes; at the same film thickness values, the velocity standard deviation is maximized. This local augmentation can be expected, given that at the same distance away from the wall, substantially higher velocities ensue in the flow fields underneath the wave crests compared to flatter substrate regions. The next section is therefore devoted to the methodology developed for the study of flow fields underneath the solitary and capillary wave regions.

4.3. Wave/phase-locked flow-field averaging

The velocity fields within the quasi-periodic wave regions are examined by suitably averaging instantaneous PTV velocity maps. In order to identify which images can be used in the averaging procedure and by how much each one would need to be translated along the axial/streamwise direction so as to match a desired interfacial topology, the following procedure is adopted: (i) a film profile (instantaneous spatial film-thickness trace such as Fig. 8 (top)) pertaining to the desired wave topology is selected, referred to as the reference signal; (ii) this signal is then cross-correlated with all available instantaneous film-thickness traces from the same data set (flow condition), and a mean translation value is obtained for each image/signal pair; (iii) an absolute translation limit is imposed (set to 80 pixels in this work), and all signals satisfying this condition are translated and averaged.

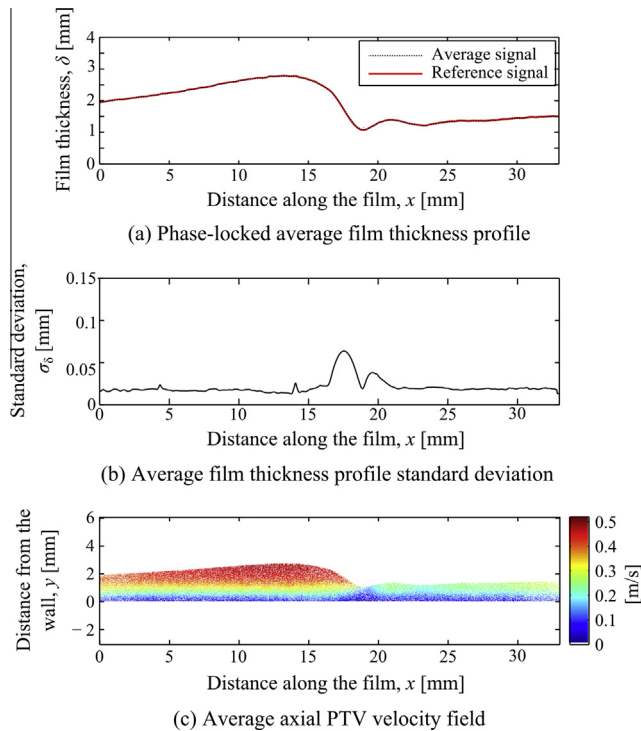


Fig. 16. (a) Sample reference and averaged film wave profiles for $Re = 27$, $Ka = 85$ and 10 Hz forcing frequency. (b) Standard deviations calculated at all axial locations along the reference profile. (c) Phase-locked average axial velocity map corresponding to the average film thickness profile of plot (a).

A sample initial reference signal and final average film-thickness trace (for $Re = 27$, $Ka = 85$ and a forcing frequency of 10 Hz) are presented in Fig. 16(a). This average film-thickness trace was generated by averaging 96 instantaneous film-thickness traces. As a qualitative error estimator of the averaging procedure, standard deviations were calculated at all axial locations along the reference signal (Fig. 16(b)), peaking at approximately 60 μm in the region bounded by the wave crest and trough. The capillary wave and flatter regions displayed values of around 40 and 20 μm . The magnitudes of these deviations, and in particular the deviations associated with regions where local maxima are observed, depend to some extent on the selected limiting value for the translation. Increasing this value allows for the utilization of a larger number of signals, with only a “mild” effect on local errors; doubling, for example, the originally employed limiting value results in nearly double the number of signals available for averaging, and only causes an increase of roughly 15% in the peak deviation. Despite the fact that local deviations are only modestly increased, the introduction of “smearing” in certain regions (mainly the capillary wave zone) is a clear downside of the employment of a larger number of signals. For this reason, the displacements obtained by setting a “tight” 80 pixel translation limit were employed in rearranging instantaneous PTV velocity and obtaining the corresponding average velocity field presented in Fig. 16(c).

An inherent strength of the presently adopted method is that velocity information can be extracted from any desired location along the wave topology, thus allowing for direct, locally resolved comparisons to analytical or numerical data, further facilitating the investigation of the effect of waviness on the dynamics of falling films. Following the average PTV velocity-field generation (Fig. 16(d)), the evolution of axial velocity profiles from the back of the wave, to the wave crest, and along the capillary wave and flat-film regions will now be examined in detail. In Fig. 17, velocity

profiles along the average film-thickness trace are extracted at 20 successive spatial stations, separated by 1.6 mm. Each profile is evaluated by further averaging along a 228 μm domain (8 vectors) in the streamwise direction; recall that nominal resolution of this measurement is 28.6 μm . In addition to the profiles retrieved by the experiment, corresponding analytically derived (Nusselt) profiles have also been plotted. The following observations can be made by inspection of the results:

- (i) Profiles in the capillary wave and substrate regions (the regions ahead of the main wave) display significantly lower (by up to 40%) interfacial velocities compared to the thicker wave region.
- (ii) The experimentally derived axial velocity profiles are generally parabolic in shape like the Nusselt profiles, apart from Profile 11 that corresponds to the sloping region between the wave crest and trough. This observation is consistent with results from other flow conditions.
- (iii) No negative axial velocities (backflow in an absolute reference frame) or recirculation zones were encountered under or ahead of the wave in the range of investigated flows, an observation consistent with results presented by other researchers, for example [40] for unfurced Silicone Fluid 200 ($Ka = 18.4$) films flowing down a 45° inclined flat plate ($Re = 11$ –220), and Adomeit and Renz [46], for Dimethylsulfoxide (DMSO) vertically falling films ($Re = 27$ –200). Despite the fact that the fluid properties and experimental conditions of both aforementioned studies are different to the presently examined ones, some interesting similarities appear upon comparison.
- (iv) The PTV-derived and Nusselt-profile data in the present study ($Re = 27$, $Ka = 85$ and 10 Hz forcing frequency) are in excellent agreement with the photochromic-dye trace and Nusselt profile data presented by Moran et al. [40] ($Re = 26$, $Ka = 18.54$), regarding the evolution and relative deviations between experiments and analytical solutions. In particular, Moran et al. [40] showed that the Nusselt velocity profiles over-predicted their direct experimental velocity data by about 30% behind the wave crests and up to 100% at the wave crests, while agreeing to within 10% in the flat-film regions. In fact, ahead of and in close vicinity to the waves, the experimental data were under-predicted by the Nusselt solution. In the present effort, we observe that the PTV-derived interfacial velocity is nearly matched at the measurement location furthest away from the wave crest (Profile 1), with a deviation growing progressively (10% lower interfacial velocity for the experimental result), reaching 70% at the crest (Profile 8) and then becoming slightly negative (by up to 25% for Profiles 13–20). For a flow with $Re = 30$ and a fluid with $Ka = 1042$, Adomeit and Renz [46] reported 25–40% lower velocities by the application of micro-PIV underneath the wave crests in comparison to Nusselt predictions, but higher velocities in all other regions, and in particular the back of the wave.

We consider now a flow with nearly the same Re (25 compared to 27), the same Ka , and a forcing frequency of 7 Hz. Over the entire range of Re and Ka examined in the present experimental campaign, given the same flow Re and Ka , reducing the forcing frequency from 10 Hz to 7 Hz or 5 Hz consistently results in both higher wave to mean film height and wave to substrate height ratios (similar trends can be observed at higher frequencies, such as those presented by Dietze et al. [33]). For the particular flow pair considered here, the maximum to mean film height increases from 1.5 to 1.7 and the film thickness standard deviation (flow waviness) rises from 0.48 mm to 0.56 mm. It has been established in

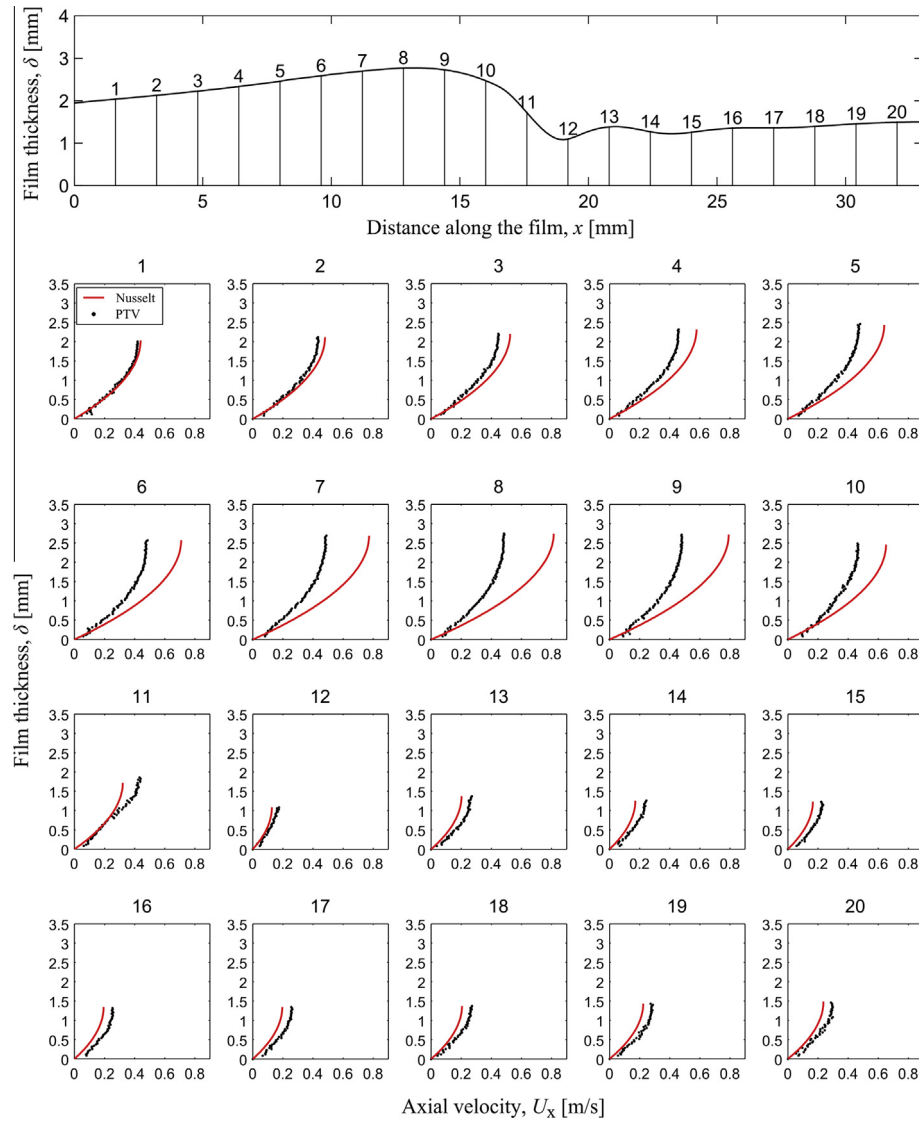


Fig. 17. Averaged wave profile for a wavy film flow pertaining to $Re = 27$, $Ka = 85$ and 10 Hz forcing frequency (Fig. 16(a)), presented along with axial velocity profiles extracted from 20 locations along the wave topology. The spatial separation between the profiles is 1.6 mm, while the spatial resolution across the film height corresponds to the apparent spatial resolution of the imaging setup ($28.6 \mu\text{m}$). Analytically derived parabolic profiles at the same locations were calculated according to the Nusselt relation and are plotted along with the experimental data points.

the literature that enhancing the waviness of unforced films, for example by increasing the Re , results in higher mass fractions being transported by the waves (Moran et al. [40]), and larger deviations between the Nusselt and experimental profiles derived from underneath the wave crests (Karimi and Kawaji [38]). In reference to the work of the previously noted authors, Adomeit and Renz [46], for example, reported deviations of up to 50% for $Re = 77$ compared to 25–40% for $Re = 30$. The effect of increased waviness (by modulating the wave frequency) on the axial velocity profile evolution in harmonically excited film-flows, as well as its deviations from local Nusselt profiles along the wave, is hereby examined, to our knowledge, for the first time (Fig. 18):

- (i) As before, parabolic axial velocity profiles are encountered throughout the investigated flow field, apart from Profile 11, and in this flow case, Profile 12 as well.
- (ii) The nature of the discrepancies between the local measured velocity profiles and corresponding Nusselt solutions, and their dependence on the shape of the interface and flow Re , is of particular interest for the modelling of these flows.

It may be speculated that they can be traced back to the flow two-dimensionality presented in Fig. 16(d), and in particular, the region to the left of the wave trough. The trough displays the lowest axial velocity values across the local film height compared to any other region of the flow, with higher values being gradually observed while moving towards the domain below the wave crest. Our data also indicate the presence of non-zero cross-stream velocity components (liquid movement towards the gas–liquid interface) in the two locations where deviations from the parabolic profile shape are most notably observed, an effect believed to be inherently linked to the local deceleration of the flow along the streamwise direction.

- (iii) PTV-derived velocities are considerably over-predicted by the Nusselt solution, the over-prediction being worse than in the higher frequency (10 Hz) flow at all locations up to the wave crest. For example, the interfacial velocity deviation between Profile 1 and the Nusselt solution is 23%, increasing to nearly 100% for Profiles 8 and 9 (compared to roughly 70% in the previous study case). Ahead of the wave

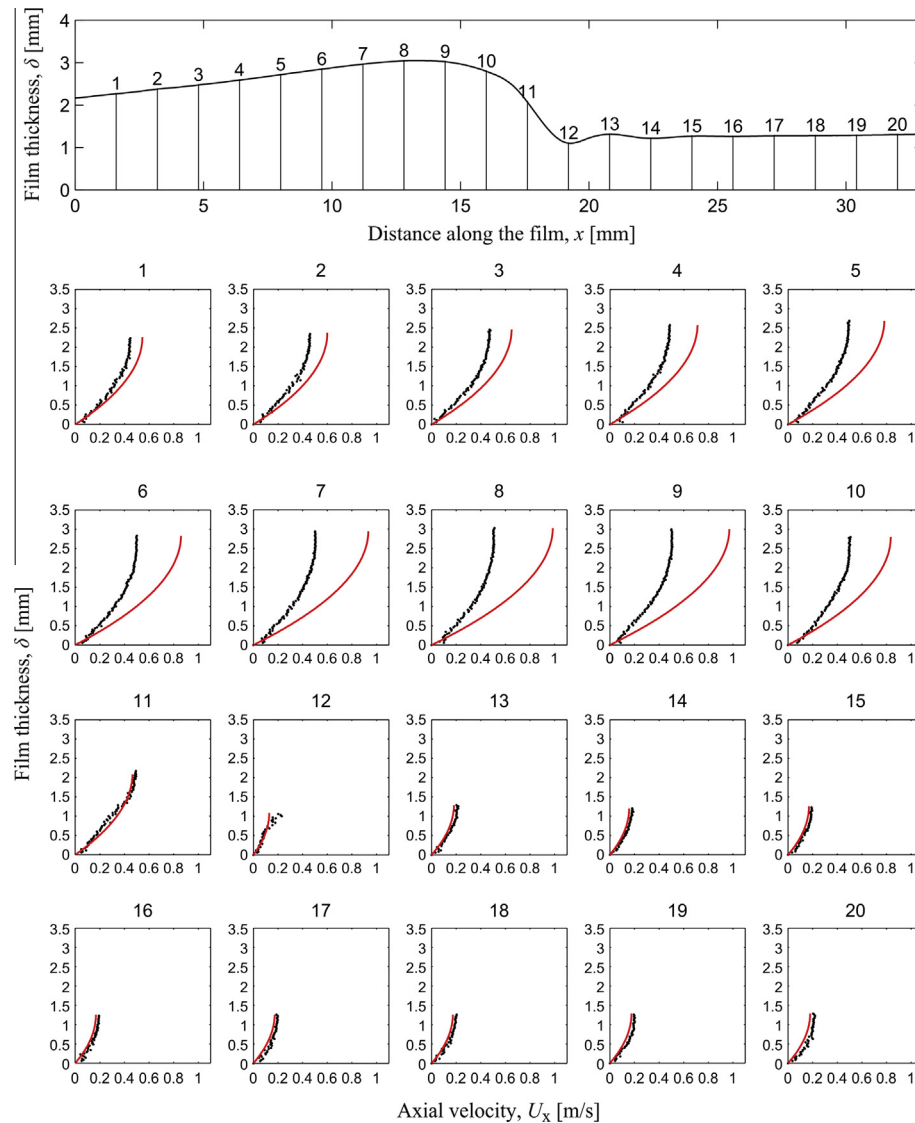


Fig. 18. Averaged wave profile for a wavy film flow pertaining to $Re = 25$, $Ka = 85$ and 7 Hz forcing frequency, presented along with axial velocity profiles and their analytically derived counterparts in the same manner as those of Fig. 17. The spatial separation between the profiles and spatial resolution across the film height are also carried over.

trough, (Profiles 13–20), the experimental data match the analytical data to within 10%, in contrast to the considerably higher under-prediction (by around 25%) encountered previously.

In reference to the 5 Hz study for $Re = 25$ and the same Ka (a plot including the results of this analysis is not presented here), the maximum to mean height ratio corresponds to 1.8, the film thickness standard deviation to 0.52 mm, and the results of the velocity profile evolution along and ahead of the wave are in excellent agreement with the 7 Hz case.

5. Conclusions

A simultaneous measurement technique based on planar laser-induced fluorescence imaging (PLIF) and particle image/tracking velocimetry (PIV/PTV) was developed and applied for the investigation of the hydrodynamic characteristics of harmonically excited liquid thin-film flows. The technique was developed as part of an experimental campaign that considered four different Ka -number liquids, Re numbers spanning the range 2.3–320, and

(inlet-forced) wave frequencies in the range 1–10 Hz. PLIF was employed in order to produce spatiotemporally resolved film thickness measurements and mask out particle reflections in the raw particle images. The latter were then processed using a multi-pass cross-correlation approach in order to generate 2-D PIV velocity-vector maps of the flowfield underneath the wavy interface. PTV was implemented as a final processing step, in order to enhance the spatial resolution of the velocity measurements and moderate the effect of bias errors in regions of the flow characterized by strong velocity gradients.

A series of experiments were conducted in order to assess the validity of the combined optical technique. First, film thickness data from flat (unforced) films ($Ka = 14$) were compared to micrometer stage measurements, as well as the 1-D, steady, fully developed Nusselt solution. The resulting deviations were around 20 μm for both tests; less than the nominal resolution of the imaging system. Relative deviations were calculated between PTV derived interfacial and bulk velocities and analytical results, with mean values amounting to 3.2% for both test cases. Finally, flow rate comparisons were conducted between PLIF/PTV-derived and flowmeter data of liquid flow rates. The mean

relative deviation was 1.6% for a total of six flat and nine wavy flows.

After providing a detailed account of the experimental methodology, wave/phase locked flow-field averaging was introduced and implemented in order to study the role of waviness on these harmonically excited film flows. This particular approach allows the generation of highly localized velocity profile, bulk velocity and flow rate data along the wave topology. In the present contribution, velocity profiles were extracted from 20 locations along the wave topology and compared to analytically calculated ones based on local film thickness measurements and the Nusselt solution. The following deductions can be made, based on the results of this analysis:

- (i) Increasing the waviness of the films by modulating the forcing frequency leads to lower absolute deviations between the experimental data and theoretical Nusselt predictions ahead of the wave crests, and higher deviations behind the wave crests. At the wave crests, experimentally derived interfacial velocities are overestimated by nearly 100%. It would be interesting to extend this analysis in the future to include locally resolved flow rate data over a wide range of harmonically excited film flow conditions (in terms of the Ka and Re numbers, and the forcing frequency) in order to elucidate the link between the mass transfer characteristics of film flows and the film height (see for example Alekseenko et al. [3] who studied the effect of waviness on CO_2 absorption). The same conclusion applies to the observation of locally non-parabolic profiles ahead of the wave crests and their potential link to the cross-stream velocity field.
- (ii) The effectiveness of the proposed simultaneous application of fluorescence imaging and particle velocimetry for the detailed investigation of liquid-film flows has been demonstrated successfully, and a strong case has been made in support of the thesis that novel information can arise by its employment in the analysis of the interfacial wave dynamics, while also providing much needed 2-D velocity data for the development and validation of advanced models of these flows.

Acknowledgement

This work was supported by the Engineering and Physical Sciences Research Council (EPSRC), UK [Grant number EP/K008595/1].

References

- [1] N. Brauner, D.M. Maron, Characteristics of inclined thin films, waviness and the associated mass transfer, *Int. J. Heat Mass Transfer* 25 (1) (1982) 99–110.
- [2] I. Mudawar, R.A. Hout, Measurement of mass and momentum transport in wavy-laminar falling liquid films, *Int. J. Heat Mass Transfer* 36 (17) (1993) 4151–4162.
- [3] S.V. Alekseenko, V.E. Nakoryakov, B.G. Pokusaev, Wave effect on the transfer processes in liquid films, *Chem. Eng. Commun.* 141–142 (1996) 359–385.
- [4] S. Ishigai, S. Nakanishi, Hydrodynamics and heat transfer of vertical falling liquid films (part 1, classification of flow regimes), *Bull. JSME* 15 (83) (1972) 594–602.
- [5] T. Ueda, H. Tanaka, Measurements of velocity, temperature and velocity fluctuation distributions in falling liquid films, *Int. J. Multiphase Flow* 2 (1975) 261–272.
- [6] T.H. Lyu, I. Mudawar, Statistical investigation of the relationship between interfacial waviness and sensible heat transfer to a falling liquid film, *Int. J. Heat Mass Transfer* 34 (6) (1991) 1451–1464.
- [7] T. Nosoko, P.N. Yoshimura, T. Nagata, K. Oyakawa, Characteristics of two-dimensional waves on a falling liquid film, *Chem. Eng. Sci.* 51 (5) (1996) 725–732.
- [8] T.D. Karapatsios, S.V. Paras, A.J. Karabelas, Statistical characteristics of free falling films at high Reynolds numbers, *Int. J. Multiphase Flow* 15 (1) (1989) 1–21.
- [9] R.J. Belt, J.M.C. Van't Westende, H.M. Prasser, L.M. Portela, Time and spatially resolved measurements of interfacial waves in vertical annular flow, *Int. J. Multiphase Flow* 36 (2010) 570–587.
- [10] Y.Q. Yu, S.J. Wei, Y.H. Yang, X. Cheng, Experimental study of water film falling and spreading on a large vertical plate, *Prog. Nucl. Energy* 54 (2012) 22–28.
- [11] W. Ambrosini, N. Forgiione, F. Oriolo, Statistical characteristics of a water film falling down a flat plate at different inclinations and temperatures, *Int. J. Multiphase Flow* 28 (2002) 1521–1540.
- [12] Y. Zhao, C.N. Markides, O.K. Matar, G.F. Hewitt, Disturbance wave development in two-phase gas-liquid upwards vertical annular flow, *Int. J. Multiphase Flow* 55 (2013) 111–129.
- [13] A. Schagen, M. Modigell, Luminescence technique for the measurement of local concentration distribution in thin liquid films, *Exp. Fluids* 38 (2005) 174–184.
- [14] A. Schagen, M. Modigell, G. Dietze, R. Kneer, Simultaneous measurement of local film thickness and temperature distribution in wavy liquid films using a luminescence technique, *Int. J. Heat Mass Transfer* 49 (2006) 5049–5061.
- [15] A. Schagen, M. Modigell, Local film thickness and temperature distribution measurement in wavy liquid films with a laser-induced luminescence technique, *Exp. Fluids* 43 (2007) 209–221.
- [16] J. Liu, J.D. Paul, J.P. Gollub, Measurements of primary instabilities of film flows, *J. Fluid Mech.* 250 (1993) 69–101.
- [17] J. Liu, J.P. Gollub, Solitary wave dynamics of film flows, *Phys. Fluids* 6 (5) (1994) 1702–1712.
- [18] J. Liu, J.P. Gollub, Onset of spatially chaotic waves on flowing films, *Phys. Rev. Lett.* 70 (15) (1993) 2289–2292.
- [19] J. Liu, J.B. Schneider, J.P. Gollub, Three-dimensional instabilities of film flows, *Phys. Fluids* 7 (1) (1994) 55–67.
- [20] M. Vlachogiannis, V. Bontozoglou, Observations of solitary wave dynamics of film flows, *J. Fluid Mech.* 435 (2001) 191–215.
- [21] S.V. Alekseenko, V.A. Antipin, V.V. Guzanov, S.M. Kharlamov, D.M. Markovich, Three-dimensional solitary waves on falling liquid film at low Reynolds numbers, *Phys. Fluids* 17 (2005) 121701–121704.
- [22] S. Alekseenko, A. Cherdantsev, M. Cherdantsev, S. Isaenkov, S. Kharlamov, D. Markovich, Application of a high-speed laser-induced fluorescence technique for studying the three-dimensional structure of annular gas-liquid flow, *Exp. Fluids* 53 (2012) 77–89.
- [23] S. Alekseenko, V. Antipin, A. Cherdantsev, S. Kharlamov, D. Markovich, Two-wave structure of liquid film and wave interrelation in annular gas-liquid flow with and without entrainment, *Phys. Fluids* 21 (6) (2009) 061701–1–061701–4.
- [24] S. Alekseenko, A. Cherdantsev, M. Cherdantsev, D. Markovich, Investigation of secondary waves dynamics in annular gas-liquid flow, *Microgravity Sci. Technol.* 21 (Suppl 1) (2009) S221–S226.
- [25] A.V. Cherdantsev, D.B. Hann, B.J. Azzopardi, Study of gas-sheared liquid film in horizontal rectangular duct using high-speed LIF technique: Three-dimensional wavy structure and its relation to liquid entrainment, *Int. J. Multiphase Flow* 67 (2014) 52–64.
- [26] I. Zadrzil, O.K. Matar, C.N. Markides, An experimental characterization of downwards gas-liquid annular flow by laser-induced fluorescence: Flow regimes and film statistics, *Int. J. Multiphase Flow* 60 (2014) 87–102.
- [27] R.G. Morgan, C.N. Markides, C.P. Hale, G.F. Hewitt, Horizontal liquid-liquid flow characteristics at low superficial velocities using laser-induced fluorescence, *Int. J. Multiphase Flow* 43 (2012) 101–117.
- [28] R. Mathie, H. Nakamura, C.N. Markides, Heat transfer augmentation in unsteady conjugate thermal systems – Part II: Applications, *Int. J. Heat Mass Transfer* 56 (2013) 819–833.
- [29] R. Mathie, A. Charogiannis, C.N. Markides, Combined PLIF-IR thermal measurements of wavy film flows undergoing forced harmonic excitation, in: 10th International Conference on Heat Transfer, Fluid Mechanics and Thermodynamics, Orlando, Florida, 14–16 July, 2014.
- [30] P. Chamrath, S.V. Garimella, S.T. Wereley, Measurement of the temperature non-uniformity in a microchannel heat sink using microscale laser induced fluorescence, *Int. J. Heat Mass Transfer* 53 (2010) 3275–3283.
- [31] V.V. Le, F. Al-Sibai, A. Leefken, U. Renz, Local thickness and wave velocity measurement of wavy films with a chromatic confocal imaging method and a fluorescence intensity technique, *Exp. Fluids* 39 (2005) 856–864.
- [32] G.F. Dietze, A. Leefken, R. Kneer, Investigation of the backflow phenomenon in falling liquid films, *J. Fluid Mech.* 595 (2008) 435–459.
- [33] G.F. Dietze, F. Al-Sibai, R. Kneer, Experimental study of flow separation in laminar falling liquid films, *J. Fluid Mech.* 637 (2009) 73–104.
- [34] A.T. Popovich, R.L. Hummel, A new method for non-disturbing turbulent flow measurements very close to a wall, *Chem. Eng. Sci.* 22 (1967) 21–25.
- [35] F.C.K. Ho, R.L. Hummel, Average velocity distributions within falling liquid films, *Chem. Eng. Sci.* 25 (1970) 1225–1237.
- [36] G. Karimi, M. Kawaji, Flooding in vertical counter-current annular flow, *Nucl. Eng. Des.* 200 (2000) 95–105.
- [37] M. Kawaji, W. Ahmad, J.M. DeJesus, B. Sutharshan, C. Lorencez, M. Ojha, Flow visualization of two-phase flows using photochromic dye activation method, *Nucl. Eng. Des.* 141 (1993) 343–355.
- [38] G. Karimi, M. Kawaji, An experimental study of freely falling films in a vertical tube, *Chem. Eng. Sci.* 53 (20) (1998) 3501–3512.

- [39] G. Karimi, M. Kawaji, Flow characteristics and circulatory motion in wavy falling films with and without counter-current gas flow, *Int. J. Multiphase Flow* 25 (1999) 1305–1319.
- [40] K. Moran, J. Inumaru, M. Kawaji, Instantaneous hydrodynamics of a laminar wavy liquid film, *Int. J. Multiphase Flow* 28 (2002) 731–755.
- [41] M. Raffel, C.E. Willert, S.T. Wereley, J. Kompenhans, *Particle Image Velocimetry: A Practical Guide*, second ed., Springer, Berlin, 2007.
- [42] S.V. Alekseenko, V.E. Nakoryakov, B.G. Pokusaev, Wave formation on a vertical falling liquid film, *AIChE J.* 31 (9) (1985) 1446–1460.
- [43] D. Schubring, R.E. Foster, D.J. Rodríguez, T.A. Shedd, Two-zone analysis of wavy two-phase flow using micro-particle image velocimetry (micro-PIV), *Meas. Sci. Technol.* 20 (2009) 1–11.
- [44] R.G. Morgan, C.N. Markides, I. Zadrazil, G.F. Hewitt, Characteristics of horizontal liquid–liquid flows in a circular pipe using simultaneous high-speed laser-induced fluorescence and particle velocimetry, *Int. J. Multiphase Flow* 49 (2013) 99–118.
- [45] S.V. Alekseenko, V.A. Antipin, A.V. Bobylev, D.M. Markovich, Application of PIV to velocity measurements in a liquid film flowing down an inclined cylinder, *Exp. Fluids* 43 (2007) 197–207.
- [46] P. Adomeit, U. Renz, Hydrodynamics of three-dimensional waves in laminar falling films, *Int. J. Multiphase Flow* 26 (2000) 1183–1208.
- [47] I. Zadrazil, C.N. Markides, An experimental characterization of liquid films in downwards co-current gas–liquid annular flow by particle image and tracking velocimetry, *Int. J. Multiphase Flow* 68 (2014) 1–12.
- [48] A.C. Ashwood, S.J. Vanden Hogen, M.A. Rodarte, C.R. Kopplin, D.J. Rodríguez, E.T. Hurlburt, A multiphase, micro-scale PIV measurement technique for liquid film velocity measurements in annular two-phase flow, *Int. J. Multiphase Flow* 68 (2015) 27–39.
- [49] R. Budwig, Refractive index matching methods for liquid flow investigations, *Exp. Fluids* 17 (5) (1994) 350–355.
- [50] Y.M. Zhu, V. Kaftandjian, G. Peix, D. Babot, Modulation transfer function evaluation of linear solid-state X-ray-sensitive detectors using edge techniques, *Appl. Opt.* 34 (22) (1995) 4937–4943.
- [51] C.J. Kähler, S. Scharnowski, C. Cierpka, On the uncertainty of digital PIV and PTV near walls, *Exp. Fluids* 52 (2012) 1641–1656.
- [52] C.J. Kähler, S. Scharnowski, C. Cierpka, On the resolution limit of digital particle image velocimetry, *Exp. Fluids* 52 (2012) 1629–1639.
- [53] C.J. Kähler, U. Scholz, J. Ortmanns, Wall-shear-stress and near-wall turbulence measurements up to single pixel resolution by means of long-distance micro-PIV, *Exp. Fluids* 41 (2006) 327–341.
- [54] W. Nusselt, Die Oberflächenkondensation des Wasserdampfes, *Z. Vereines Deutscher Ingenieure* 60 (1916) 541–546.
- [55] R.D. Keane, R.J. Adrian, Optimization of particle image velocimeters. I. Double pulsed systems, *Meas. Sci. Technol.* 1 (11) (1990) 1202–1215.
- [56] R.D. Keane, R.J. Adrian, Theory of cross-correlation analysis of PIV images, *Appl. Sci. Res.* 49 (3) (1992) 191–215.